

Quantum states in disordered media. II. Spatial charge carrier distributionA. V. Nenashev,^{1,*} S. D. Baranovskii^{1,2,†}, K. Meerholz,² and F. Gebhard^{1,‡}¹*Department of Physics and Material Sciences Center, Philipps-Universität Marburg, D-35032 Marburg, Germany*²*Department für Chemie, Universität zu Köln, Luxemburger Straße 116, 50939 Köln, Germany*

(Received 5 December 2022; accepted 10 February 2023; published 24 February 2023)

The space- and temperature-dependent electron distribution $n(\mathbf{r}, T)$ is essential for the theoretical description of the optoelectronic properties of disordered semiconductors. We present two powerful techniques to access $n(\mathbf{r}, T)$ without solving the Schrödinger equation. First, we derive the density for nondegenerate electrons by applying the Hamiltonian recursively to random wave functions (RWF). Second, we obtain a temperature-dependent effective potential from the application of a universal low-pass filter (ULF) to the random potential acting on the charge carriers in disordered media. Thereby, the full quantum-mechanical problem is reduced to the quasiclassical description of $n(\mathbf{r}, T)$ in an effective potential. We numerically verify both approaches by comparison with the exact quantum-mechanical solution. Both approaches prove superior to the widely used localization landscape theory (LLT) when we compare our approximate results for the charge carrier density and mobility at elevated temperatures obtained by RWF, ULF, and LLT with those from the exact solution of the Schrödinger equation.

DOI: [10.1103/PhysRevB.107.064207](https://doi.org/10.1103/PhysRevB.107.064207)**I. INTRODUCTION**

Short-range disorder potentials govern the optoelectronic properties of a wide variety of disordered materials designed for applications in modern electronics [1]. In this work we address the theoretical description of the energetically low-lying, spatially localized states in several classes of disordered materials.

One broad class of widely studied disordered materials are semiconductor alloys with electronic states localized by a short-range disorder potential. Alloys are crystalline semiconductors, such as $A_{\bar{x}}B_{1-\bar{x}}$, whose lattice sites are occupied in a given proportion \bar{x} by chemically different isoelectronic atoms, A and B . Research on semiconductor alloys currently experiences a renaissance because alloying is one of the most efficient tools to adjust material properties for device applications. For example, alloying permits one to tune lattice constants, effective masses of charge carriers, and, most importantly, the band-structure of the underlying semiconductor. In particular, band gaps in alloy semiconductors are sensitive to the mole fractions \bar{x} and $1 - \bar{x}$ of the alloy components. Since the band gap is a key property responsible for light absorption and emission, band-gap tunability in a wide energy range opens rich perspectives for applications of alloy semiconductors in various optoelectronic devices. Over recent years, this band-gap engineering has been applied to nitride semiconductors used in modern LEDs [2], to perovskites for

applications in photovoltaics [3,4], and to two-dimensional systems, such as transition metal dichalcogenides, desired to miniaturize the corresponding devices toward nearly atomically thin dimensions [5,6].

Another class of disordered materials with short-range disorder potentials are amorphous oxide semiconductors, such as InGaZnO, desired for applications in thin-film transistors for transparent and flexible flat-panel displays [7,8]. Also traditional amorphous semiconductors, such as hydrogenated amorphous silicon, hydrogenated amorphous carbon, polycrystalline and micro-crystalline silicon, belong to disordered materials, whose optoelectronic properties are governed by short-range disorder potentials. Such amorphous semiconductors are desired for applications in Schottky barrier diodes, pin diodes, thin-film transistors, and thin-film solar cells [1].

Besides their unique properties favorable for device applications, materials with short-range disorder are advantageous systems for developing and testing theoretical descriptions of disorder effects. The compositional fluctuations in alloys and structural short-range fluctuations in oxide and amorphous semiconductors cause spatial fluctuations of the band gap which creates a random potential acting on electrons and holes. The isoelectronic substitution of the alloy components and/or amorphous atomic structure creates a short-range fluctuating crystal potential, and the physics is not complicated by long-range effects. The random potential leads to the spatial localization of charge carriers in electron states at low energies that dominate the optoelectronic properties of disordered semiconductors. Therefore, the low-energy localized electron states require an appropriate theoretical description.

Already in the 1960s, a powerful theoretical tool to calculate the density of low-energy localized states (DOS) without solving the Schrödinger equation was developed by Halperin and Lax [9]. They recognized that the spatial spread of wave

*On leave of absence from Rzhanov Institute of Semiconductor Physics and the Novosibirsk State University, Russia; nenashev_isp@mail.ru

[†]sergei.baranovskii@physik.uni-marburg.de

[‡]florian.gebhard@physik.uni-marburg.de

functions even in the low-energy localized states is much broader than the spatial scale of the fluctuations in the random potential $V(\mathbf{r})$. Hence, they proposed to apply a filter to smooth $V(\mathbf{r})$ where the absolute square of the wave function serves as the filter function [9]. Later, Baranovskii and Efros [10] addressed the same problem by a slightly different variational technique and confirmed the result of Halperin and Lax for the low-energy tail of the DOS. Theoretical studies have been performed for various kinds of disordered semiconductors that focus on the averaged DOS, leaving aside the temperature-dependent spatial distribution of the electron density $n(\mathbf{r}, T)$. However, the knowledge of $n(\mathbf{r}, T)$ in a random potential is required to study theoretically charge transport and light absorption/emission in disordered semiconductors.

The distribution $n(\mathbf{r}, T)$ is obtained from the solution of the Schrödinger equation in the presence of a disorder potential. However, solving the Schrödinger equation is extremely demanding with respect to computational time and computer memory. It is hardly affordable for applications to realistically large chemically complex systems. Therefore, theoretical tools to obtain the essential features of localized states without solving the Schrödinger equation are highly desirable.

One of such tools is the recently introduced “localization landscape theory” (LLT) [11–14]. The LLT is widely considered as one of the efficient theoretical approaches to calculate the local density of states in disordered systems, for instance, in light-emitting diodes [2,15–21] and in photodetectors [22,23]. The LLT has been used to simulate the carrier effective potential fluctuations induced by alloy disorder in InGaN/GaN core-shell microrods [24]. Furthermore, the LLT has been applied to compute the eigenstate localization length at very low energies in a two-dimensional disorder potential [25]. The LLT is sometimes considered capable to reveal errors in the finite element method software in applications to alloys [26]. The LLT is an important ingredient for calculating quantum corrections in drift-diffusion models [27–29]. It has been used for the computation of light absorption in three-dimensional InGaN alloys of different compositions [30] and in mixed halide perovskites [31].

The LLT is based on a mathematical theory of quantum localization that introduces an effective localization potential. Using the effective potential, the quantum mechanical problem reduces to a quasiclassical description of charge carriers localized in the effective potential landscape. This allows the prediction of localization regions for electrons and holes, of their corresponding energy levels, and of the (local) densities of states. The effective potential can be directly implemented in a drift-diffusion model of carrier transport and into the calculation of absorption/emission transitions so that physical features on a mesoscopic scale become accessible.

In the preceding paper [32], it was shown that the LLT becomes equivalent to the low-pass filter approach of Halperin and Lax [9] for the specific case of a Lorentzian filter when applied to the Schrödinger equation with a constant mass. In this work, we propose two recipes for calculating $n(\mathbf{r}, T)$ in disordered systems without solving the Schrödinger equation, both of them prove to be superior to the LLT.

The first recipe is the random-wave-function (RWF) algorithm described in Sec. II C. In this approach, many sets of random wave functions are generated for a given realization of the potential $V(\mathbf{r})$ acting on the charge carriers. Such procedure has been suggested by Lu and Steinerberger [33] to search for the low-lying eigenfunctions of various linear operators. After a repeated application of the thermal operator, the temperature-dependent electron density is found from averaging the results over different sets. This procedure provides reliable results for $n(\mathbf{r}, T)$ for fairly large systems. The RWF approach has the following advantages over the LLT. While the output of the LLT depends on the choice of an adjustable parameter that can be found only by comparison with the exact solution, the RWF scheme does not contain any adjustable parameters. Furthermore, the accuracy of the RWF approach for computing $n(\mathbf{r}, T)$ can be improved systematically, whereas the accuracy of the LLT is limited by construction. Moreover, all temperatures are accessible for the RWF algorithm, whereas LLT is valid only at sufficiently high T , as discussed in Sec. IV.

The second recipe employs an effective temperature-dependent potential $W(\mathbf{r}, T)$ that permits a quasiclassical calculation of the particle density. The effective potential is obtained from the random potential $V(\mathbf{r})$ by applying a universal low-pass filter (ULF), as described in Sec. III D 3. This approach resembles the one suggested by Halperin and Lax [9]. In our work, we use a low-pass filter to compute the spatial electron distribution $n(\mathbf{r}, T)$ while Halperin and Lax and their successors focused on the features of the averaged DOS. The ULF algorithm is equivalent to the LLT inasmuch it replaces the random potential V by an effective potential W that is used for a quasiclassical description of the electron distribution. However, the ULF scheme of converting V into W principally differs from the LLT scheme. While LLT is based on solving a system of algebraic equations, the ULF algorithm employs Fast-Fourier Transformation to calculate the effective potential W so that very large systems can be addressed. More importantly, the ULF description leads to an explicit temperature dependence of the effective potential, $W \equiv W(\mathbf{r}, T)$. On the contrary, the effective potential in LLT does not depend on T . This feature is the main disadvantage of the LLT as compared to the ULF algorithm. Consequently, the range of applicability for the ULF scheme is much broader than that for the LLT, as illustrated in Sec. IV. Typically, the ULF description encompasses the experimentally accessible temperature regime.

In our theoretical consideration, we consider electrons as noninteracting particles. Commonly, electron-electron interactions are taken into account in the self-consistent solution of the Schrödinger equation and Poisson equation. Since we suggest to replace the solution of the Schrödinger equation in search for $n(\mathbf{r}, T)$ by RWF or ULF techniques, the latter methods should be exploited in a self-consistent combination with the Poisson equation to simulate realistic conditions met in devices.

Our paper is structured as follows. In Sec. II, we develop the RWF algorithm to calculate $n(\mathbf{r}, T)$ for dilute charge carriers in disordered media.

In Sec. III, we derive the temperature-dependent effective potential $W(\mathbf{r}, T)$ that permits a semiclassical description of

the particle density. The algorithm employs a ULF function and a temperature-dependent shift that we derive and analyze in detail.

The space- and temperature-dependent electron distribution $n(\mathbf{r}, T)$ is the key ingredient for the theoretical treatment of charge transport. In Sec. IV, we analyze the results of different approaches for the particle density and for the charge carrier mobility in disordered media at elevated temperatures.

Conclusions in Sec. V close the main part of our presentation. Minor technical aspects of our work are deferred to two Appendices.

II. ELECTRON DENSITY IN DISORDERED MEDIA

In this section we develop the random-wave-function algorithm to calculate the electron density in nondegenerate systems at finite temperatures. We start with definitions in Sec. II A. Then, in Sec. II B, we express the particle density as an average over a random combination of eigenstates. In Sec. II C, we summarize the main steps of the algorithm. Finally, in Sec. II D, we illustrate the algorithm and demonstrate its efficacy for disordered systems in one, two, and three dimensions.

A. Electron density for potential problems

Let us consider a system of noninteracting electrons governed by a single-particle Hamiltonian

$$\hat{H} = \hat{T} + \hat{V}, \quad (1)$$

where \hat{T} describes their kinetic energy and \hat{V} is some potential in the specimen volume Ω . We are interested to calculate the electron density $n(\mathbf{r}, T)$ in thermal equilibrium at temperature T . The eigenstates of the Hamiltonian $|\varphi_i\rangle$ with eigenenergies ϵ_i ,

$$\hat{H}|\varphi_i\rangle = \epsilon_i|\varphi_i\rangle, \quad (2)$$

have the position-space representation $\varphi_i(\mathbf{r})$,

$$\varphi_i(\mathbf{r}) = \langle \mathbf{r} | \varphi_i \rangle, \quad (3)$$

and $|\varphi_i(\mathbf{r})|^2$ gives the probability to find the electron at \mathbf{r} in the eigenstate $|\varphi_i\rangle$. Correspondingly, the eigenfunctions are normalized by unity,

$$\int_{\Omega} |\varphi_i(\mathbf{r})|^2 d\mathbf{r} = 1, \quad (4)$$

because the electron can be found somewhere in the specimen.

In the presence of a finite number of electrons N in Ω , the electron density $n(\mathbf{r}, T)$ at temperature T is defined by

$$n(\mathbf{r}, T) = 2 \sum_i |\varphi_i(\mathbf{r})|^2 f_{\text{FD}}(\epsilon_i), \quad (5)$$

where the factor two accounts for the spin degeneracy and $f_{\text{FD}}(\epsilon)$ is the equilibrium (Fermi-Dirac) distribution function,

$$f_{\text{FD}}(\epsilon) = \frac{1}{1 + e^{\beta(\epsilon - \mu)}}, \quad (6)$$

where $\beta = 1/(k_{\text{B}}T)$ with the Boltzmann constant k_{B} and $\mu \equiv \mu(T)$ is the chemical potential. It is fixed by the condition

$$n = \frac{N}{\Omega} = \int_{\Omega} d\mathbf{r} n(\mathbf{r}, T). \quad (7)$$

In most disordered materials, the average electron density $n(\mathbf{r}, T)$ is small so that the electrons' Fermi statistics can be ignored (nondegenerate case). Then, the Fermi-Dirac distribution can be replaced by the Maxwell-Boltzmann distribution

$$f_{\text{MB}}(\epsilon) = e^{-\beta(\epsilon - \mu)}. \quad (8)$$

In the Maxwell-Boltzmann approximation we can factor out the chemical potential,

$$n(\mathbf{r}, T) = e^{\beta\mu} \tilde{n}(\mathbf{r}, T), \quad (9)$$

where the reduced electron density $\tilde{n}(\mathbf{r}, T)$ is determined only by the eigenstates $\varphi_i(\mathbf{r})$, their eigenenergies ϵ_i , and the temperature,

$$\tilde{n}(\mathbf{r}, T) = 2 \sum_i |\varphi_i(\mathbf{r})|^2 \exp(-\beta\epsilon_i). \quad (10)$$

We note in passing that the approximation of nondegenerate electrons does not hold for band-structure theory in solid-state physics. Therefore, our formalism below cannot be applied, e.g., in density-functional theory calculations.

For numerical calculations, we assume that the Hamiltonian \hat{H} is defined on a regular grid with L sites. The volume assigned to a grid node thus is $\Delta V = \Omega/L$. A wave function takes complex amplitudes on nodes of the lattice. The value $\psi(\mathbf{r})$ of some state $|\psi\rangle$ at \mathbf{r} is obtained from

$$\psi(\mathbf{r}) = \frac{1}{\sqrt{\Delta V}} \langle \mathbf{r}_n | \psi \rangle, \quad (11)$$

where \mathbf{r} is in the grid-node volume ΔV around the grid point \mathbf{r}_n .

As a consequence of the discretization, the set of eigenenergies $\{\epsilon_i\}$ is bounded within a finite range,

$$\forall i : \epsilon_{\min} \leq \epsilon_i \leq \epsilon_{\max}, \quad (12)$$

with some lower and upper bounds ϵ_{\min} and ϵ_{\max} , respectively. Generically, ϵ_{\max} is determined by the distance between grid points, whereas ϵ_{\min} is a defining property of the problem itself. We make the discretization fine enough, $L \gg 1$, so that we can safely assume that

$$|\epsilon_{\max}| \gg |\epsilon_{\min}|. \quad (13)$$

For simplicity, we assume that the Hamiltonian \hat{H} can be represented by a real symmetric matrix. To simplify the notations, we also assume that its eigenfunctions $\varphi_i(\mathbf{r})$ are real. The generalization to complex-valued Hamiltonian matrices and eigenfunctions is straightforward.

B. Analysis

Consider a set $\{c_i^{(0)}\}$ of L independent random variables, one per eigenstate $|\epsilon_i\rangle$. Each variable $c_i^{(0)}$ is taken from a normal distribution with expectation value zero and variance

unity. Thus, when we take a large number N_R of realizations R of the sets we obtain

$$\begin{aligned}\langle c_{i,R}^{(0)} \rangle_R &= \frac{1}{N_R} \sum_{R=1}^{N_R} c_{i,R}^{(0)} = 0, \\ \langle c_{i,R}^{(0)} c_{j,R}^{(0)} \rangle_R &= \frac{1}{N_R} \sum_{R=1}^{N_R} c_{i,R}^{(0)} c_{j,R}^{(0)} = \delta_{i,j}.\end{aligned}\quad (14)$$

For a given realization R , we use the random variables $c_{i,R}^{(0)}$ as coefficients to construct a wave function $\psi_R^{(0)}(\mathbf{r})$,

$$\psi_R^{(0)}(\mathbf{r}) = \sum_{i=1}^L c_{i,R}^{(0)} \varphi_i(\mathbf{r}). \quad (15)$$

Obviously, the mean value of these wave functions over many realizations vanishes,

$$\langle \psi_R^{(0)}(\mathbf{r}) \rangle_R = \sum_{i=1}^L \langle c_{i,R}^{(0)} \rangle_R \varphi_i(\mathbf{r}) = 0. \quad (16)$$

For the calculation of the two-point correlation, we assume that \mathbf{r}_n and \mathbf{r}_m are grid nodes to write

$$\begin{aligned}\langle \psi_R^{(0)}(\mathbf{r}_n) \psi_R^{(0)}(\mathbf{r}_m) \rangle_R &= \sum_{i,j} \langle c_{i,R}^{(0)} c_{j,R}^{(0)} \rangle_R \varphi_i(\mathbf{r}_n) \varphi_j(\mathbf{r}_m) \\ &= \sum_i \varphi_i(\mathbf{r}_n) \varphi_i(\mathbf{r}_m) \\ &= \frac{1}{\Delta V} \sum_i \langle \mathbf{r}_n | \varphi_i \rangle \langle \varphi_i | \mathbf{r}_m \rangle \\ &= \frac{1}{\Delta V} \langle \mathbf{r}_n | \mathbf{r}_m \rangle \\ &= \begin{cases} 1/\Delta V & \text{if } n = m, \\ 0 & \text{otherwise.} \end{cases}\end{aligned}\quad (17)$$

Here we used Eqs. (11), (14), (15), and the fact that the eigenfunctions $|\varphi_i\rangle$ form a complete orthonormal set. Equation (17) shows that the values of $\psi_R^{(0)}(\mathbf{r}_n)$ at different grid nodes are independent random variables that obey a normal distribution with expectation value equal to zero and variance equal to $1/\Delta V$.

To introduce the temperature into the problem, we consider the wave function $\psi_R(\mathbf{r})$ that is related to $\psi_R^{(0)}(\mathbf{r})$ via

$$|\psi_R\rangle = e^{-\beta\hat{H}/2} |\psi_R^{(0)}\rangle. \quad (18)$$

We expand it over the eigenfunctions $\varphi_i(\mathbf{r})$,

$$\psi_R(\mathbf{r}) = \sum_i c_{i,R} \varphi_i(\mathbf{r}), \quad (19)$$

to find the relation between the two sets of coefficients c_i and $c_i^{(0)}$. To this end we apply the operator $e^{-\beta\hat{H}/2}$ to both sides of Eq. (15) and take into account that $|\varphi_i\rangle$ are eigenstates of the Hamiltonian. This gives

$$c_{i,R} = c_{i,R}^{(0)} \exp(-\beta\epsilon_i/2). \quad (20)$$

Using Eqs. (14) and (20), we thus find that

$$\langle c_{i,R} c_{j,R} \rangle_R = \delta_{i,j} \exp(-\beta\epsilon_i). \quad (21)$$

With the help of this correlation, we find the mean value of $|\psi_R(\mathbf{r})|^2$,

$$\begin{aligned}\langle |\psi_R(\mathbf{r})|^2 \rangle_R &= \sum_{i,j} \langle c_{i,R} c_{j,R} \rangle_R \varphi_i(\mathbf{r}) \varphi_j(\mathbf{r}) \\ &= \sum_i \exp(-\beta\epsilon_i) |\varphi_i(\mathbf{r})|^2,\end{aligned}\quad (22)$$

or, comparing with Eq. (10),

$$\langle |\psi_R(\mathbf{r})|^2 \rangle_R = \frac{1}{2} \tilde{n}(\mathbf{r}, T). \quad (23)$$

Hence, the electron density can be calculated by averaging the functions $|\psi_R(\mathbf{r})|^2$ over many realizations R . This is the basic idea of the random-wave-function algorithm that we present in more detail in the next subsection.

Our algorithm requires the application of the exponential operator $\exp(-\beta\hat{H})$ to a given wave function. In practical applications, this cannot be done exactly. We use an algebraic approximation,

$$e^{-\beta\hat{H}/2} \approx (1 - \alpha\hat{H})^M, \quad (24)$$

with a natural number M equal to

$$M \approx \frac{\beta}{2\alpha}. \quad (25)$$

The parameter α can be chosen to minimize the residual error. The action of operator $\exp(-\beta\hat{H}/2)$ suppresses the high-energy components in $|\psi_R\rangle$ relative to its low-energy ones. The algebraic approximation on the right-hand side of Eq. (24) must have a similar effect, i.e., the factor $(1 - \alpha\epsilon_{\max})^M$ has to be small with respect to $(1 - \alpha\epsilon_{\min})^M$ in absolute values, thence

$$|1 - \alpha\epsilon_{\max}| < |1 - \alpha\epsilon_{\min}| \quad (26)$$

must hold. The term $\alpha\epsilon_{\min}$ can be neglected because $|\epsilon_{\min}| \ll |\epsilon_{\max}|$ due to Eq. (13). Then, the inequality (26) reduces to $-1 < 1 - \alpha\epsilon_{\max} < 1$. We note that $\epsilon_{\max} > 0$ because this quantity is determined mainly by the maximal kinetic energy in a discretized system. Therefore, we obtain the following constraints on α ,

$$0 < \alpha < \frac{2}{\epsilon_{\max}}. \quad (27)$$

However, a good approximation in Eq. (24) requires that the number M should be large. Using Eq. (25) and recalling that $\beta = 1/(k_B T)$, we can rewrite the condition $M \gg 1$ in the form

$$\alpha \ll \frac{1}{k_B T}. \quad (28)$$

Usually $k_B T \ll \epsilon_{\max}$, and, as a consequence, the stronger condition (27) overrides the weaker condition (28).

C. Synthesis: The random-wave-function algorithm

The considerations presented in the previous subsection suggest the following random-wave-function algorithm for calculating the electron density $n(\mathbf{r}, T)$ in nondegenerate non-interacting electron systems.

S1 For each grid node \mathbf{r}_n , choose a random number $\psi_R^{(0)}(\mathbf{r}_n)$ from a normal distribution with expectation value zero and variance $1/\Delta V$. All these random numbers are

chosen independently, so that the function $\psi_{\mathbf{R}}^{(0)}(\mathbf{r})$ itself represents a sample of Gaussian white noise. The set of all numbers constitutes the realization \mathbf{R} .

S2 Apply the following transformation M times,

$$\underline{\psi}^{(m)} = \underline{\psi}^{(m-1)} - \alpha \underline{H} \underline{\psi}^{(m-1)} \quad (29)$$

with $m = 1, 2, \dots, M$. Here, $\underline{\psi}^{(m)}$ is the vector that represents the wave function on the grid, and \underline{H} is the matrix representation of the Hamiltonian on the grid. Recall that M is given by Eq. (25), and α obeys the inequalities (27). In our calculations we find that

$$\alpha = \frac{1.5}{\epsilon_{\max}} \quad (30)$$

is a suitable choice.

S3 Calculate an estimate of the reduced electron density $\tilde{n}_{\mathbf{R}}(\mathbf{r}, T)$ as

$$\tilde{n}_{\mathbf{R}}(\mathbf{r}_n, T) = 2 |\psi^{(M)}(\mathbf{r}_n)|^2 \quad (31)$$

on each grid point \mathbf{r}_n .

The steps S1–S3 are carried out for a large number $N_{\mathbf{R}}$ of realizations \mathbf{R} of $\psi_{\mathbf{R}}^{(0)}(\mathbf{r})$. Then, the electron density $n(\mathbf{r}, T)$ is the arithmetic mean of the functions $\tilde{n}_{\mathbf{R}}(\mathbf{r})$ obtained for different realizations \mathbf{R} , multiplied by a chemical-potential-related factor $e^{\beta\mu}$,

$$n(\mathbf{r}, T) = e^{\beta\mu} \langle \tilde{n}_{\mathbf{R}}(\mathbf{r}, T) \rangle_{\mathbf{R}}. \quad (32)$$

The larger the number of realizations $N_{\mathbf{R}}$, the more accurate is the calculated electron density $n(\mathbf{r}, T)$. A convenient measure of the accuracy is the relative error $\Delta(\mathbf{r}, T)$,

$$\Delta(\mathbf{r}, T) = \frac{n^{\text{rwf}}(\mathbf{r}, T) - n^{\text{exact}}(\mathbf{r}, T)}{n^{\text{exact}}(\mathbf{r}, T)}, \quad (33)$$

where $n^{\text{rwf}}(\mathbf{r}, T)$ is calculated using the random-wave-function algorithm, and the exact value $n^{\text{exact}}(\mathbf{r}, T)$ is defined by Eqs. (9) and (10). As we show in Appendix A, the expectation value of Δ^2 is equal to

$$\langle [\Delta(\mathbf{r}, T)]^2 \rangle = \frac{2}{N_{\mathbf{R}}}, \quad (34)$$

i.e., the typical deviation from the exact result is not larger than $\sqrt{1/N_{\mathbf{R}}}$.

To calculate the mean value in Eq. (32), it is necessary to store the cumulative function

$$\sum_{\mathbf{R}} \tilde{n}_{\mathbf{R}}(\mathbf{r}) \quad (35)$$

in the memory, and to update it after processing of each realization \mathbf{R} .

It is easy to estimate the resources of memory and computation time (or number of operations) demanded by the random-wave-function algorithm. It is enough to store in the memory $4L$ real numbers, namely, L entries for the potential energy in the Hamiltonian, $2L$ numbers for the wave functions $\underline{\psi}^{(m)}$ and $\underline{\psi}^{(m-1)}$ at Step S2, and L values for the sum (35). Almost all computation time is spent at Step S2. It takes $\mathcal{A} \simeq LMN_{\mathbf{R}}$ operations. Indeed, applying the Hamiltonian to a wave function costs $\mathcal{O}(L)$ operations due to the fact that the potential is local and the kinetic energy is a local second

derivative. Applying the Hamiltonian repeats M times for each of $N_{\mathbf{R}}$ realizations. Let us further express the quantities L , M , and $N_{\mathbf{R}}$ via the sample volume Ω , the distance between grid points a , and the desired relative error Δ using Eqs. (25), (30), and (34),

$$L \simeq \frac{\Omega}{a^d}, \quad M \simeq \frac{\epsilon_{\max}}{k_B T} \simeq \frac{\hbar^2}{ma^2 k_B T}, \quad N_{\mathbf{R}} \simeq \frac{1}{\Delta^2}, \quad (36)$$

in a d -dimensional system. Therefore, the estimate for the number of arithmetical operations becomes

$$\mathcal{A} \simeq LMN_{\mathbf{R}} \simeq \frac{\hbar^2}{mk_B T} \frac{\Omega}{a^{d+2} \Delta^2} \quad (37)$$

when expressed in terms of physical quantities. It is important to note that our algorithm is easily parallelized because different realizations \mathbf{R} of the wave function $\psi_{\mathbf{R}}^{(0)}(\mathbf{r})$ can be processed completely independently.

D. Example: Electrons in a random potential

In this subsection we demonstrate how to use the random-wave-function algorithm.

1. White-noise potential and dimensionless units

To be definite, we consider a noninteracting electron gas in a one-dimensional (1D), a two-dimensional (2D), and a three-dimensional (3D) white-noise random potential. Such a potential $V(\mathbf{r})$ is characterized by the statistical properties

$$\langle V_{\mathbf{R}}(\mathbf{r}) \rangle_{\mathbf{R}} = 0, \quad \langle V_{\mathbf{R}}(\mathbf{r}) V_{\mathbf{R}}(\mathbf{r} + \mathbf{r}') \rangle_{\mathbf{R}} = S \delta(\mathbf{r}'), \quad (38)$$

when the average is taken over many realization \mathbf{R} of the random potential $V_{\mathbf{R}}(\mathbf{r})$. The strength of the disorder is characterized by the parameter S . The actual value of S depends on the origin of the random potential. For instance, compositional disorder in a semiconductor alloy $A_{\bar{x}}B_{1-\bar{x}}$ leads to [34]

$$S = \frac{[\alpha(\bar{x})]^2 \bar{x}(1-\bar{x})}{N}, \quad (39)$$

where N is the concentration of atoms and $\alpha_c(\bar{x}) = dE_c(\bar{x})/d\bar{x}$ for electrons, $\alpha_v(\bar{x}) = dE_v(\bar{x})/d\bar{x}$ for holes as a function of the band edge positions $E_{c,v}(\bar{x})$.

We discretize this system using a regular grid of points, equally spaced along each dimension. This is a quadratic grid in 2D, and a simple cubic grid in 3D. The distance between neighboring grid points is a . To discretize the single-particle Hamiltonian \hat{H} , we use the simplest difference scheme for the Laplacian operator,

$$\hat{H}_{\mathbf{R}} \psi(\mathbf{r}) = -\frac{\hbar^2}{2m} \sum_{s=1}^d \frac{\psi(\mathbf{r} - a\mathbf{e}_s) + \psi(\mathbf{r} + a\mathbf{e}_s) - 2\psi(\mathbf{r})}{a^2} + V_{\mathbf{R}}(\mathbf{r})\psi(\mathbf{r}), \quad (40)$$

where $\mathbf{r} \equiv \mathbf{r}_n$ is a grid point, and $\mathbf{e}_1, \dots, \mathbf{e}_d$ are unit vectors along the coordinate axes. The realization $V_{\mathbf{R}}(\mathbf{r}_n)$ of the random potential at the grid points are chosen as independent random numbers, uniformly distributed within the range

$$-\sqrt{\frac{3S}{a^d}} < V_{\mathbf{R}}(\mathbf{r}_n) < \sqrt{\frac{3S}{a^d}}. \quad (41)$$

One can easily see that this distribution satisfies the properties (38). Indeed, the discretization converts the δ function,

$$\delta(\mathbf{r} - \mathbf{r}') \rightarrow \begin{cases} 1/a^d & \text{if } \mathbf{r} \equiv \mathbf{r}_n = \mathbf{r}_m \equiv \mathbf{r}', \\ 0 & \text{if } \mathbf{r}_n \neq \mathbf{r}_m, \end{cases} \quad (42)$$

and therefore Eq. (38) takes the form $\langle V_R(\mathbf{r}_n) \rangle_R = 0$, $\langle [V_R(\mathbf{r}_n)]^2 \rangle_R = S/a^d$, and $\langle V_R(\mathbf{r}_n) V_R(\mathbf{r}_m) \rangle_R = 0$ for $\mathbf{r}_n \neq \mathbf{r}_m$. The uniform distribution (41) meets these criteria.

It is convenient to work with dimensionless quantities. We note that it is always possible to fix the values of the Planck constant \hbar , the Boltzmann constant k_B , the effective mass m , and the disorder strength S by a proper choice of physical units. So we set all these quantities to unity,

$$\hbar = k_B = m = S = 1. \quad (43)$$

To do this, we choose a physical unit of length

$$\ell_0 = \left(\frac{\hbar^4}{m^2 S} \right)^{1/(4-d)}, \quad (44)$$

and the corresponding unit of energy

$$\varepsilon_0 = \left(\frac{m^d S^2}{\hbar^{2d}} \right)^{1/(4-d)}. \quad (45)$$

Then, the unit of time is $t_0 = \hbar/\varepsilon_0$, and the unit of temperature is $T_0 = \varepsilon_0/k_B$. As an example, we mention that in a 2D system with compositional disorder, for $\alpha = 0.5$ eV, $N = 10^{15}$ cm $^{-2}$, $x = 0.5$, and $m = 0.1 m_0$, the units of length, energy, and temperature are equal to $\ell_0 = 9.6$ nm, $\varepsilon_0 = 8.3$ meV, and $T_0 = 96$ K, respectively.

In the rest of this section, the physical units are chosen such that the equalities (43) hold. The dimensionless value of the discretization step is set to $a = 0.1\ell_0$, and the dimensionless value of temperature is set to $T = T_0 \equiv 1$, unless stated otherwise. Periodical boundary conditions apply.

2. One-dimensional case

An example of the electron density distribution in a one-dimensional white-noise potential is shown in Fig. 1. For convenience, we plot the reduced density $\tilde{n}(x, T) = e^{-\beta\mu} n(x, T)$ that is independent of the chemical potential $\mu(T)$. Here, x is the coordinate along the sample, and the electrons are noninteracting. The solid orange line depicts the exact function $\tilde{n}(x, T)$, calculated from the exact eigenvectors $\varphi_i(x)$ and eigenvalues ε_i of the single-particle Hamiltonian via Eq. (10). The dashed green line and the dotted black line are the reduced electron densities calculated by our algorithm using $N_R = 20$ and $N_R = 1000$ independent realizations, respectively. As seen from the figure, even with few iterations, $N_R = 20$, the algorithm reasonably reproduces the shape of $\tilde{n}(x, T)$. With $N_R = 1000$, the electron density almost perfectly reproduces the exact result.

To quantify the accuracy of the random-wave-function algorithm with $N_R = 1000$, we calculate the distribution of the relative error Δ , as defined in Eq. (33). The histogram of Δ is represented in Fig. 2. The red line in this figure shows a Gaussian distribution with the mean-square value equal to $\sqrt{2/N_R} \approx 0.045$, according to Eq. (34). The agreement between numerical (bars) and theoretical (line) distributions

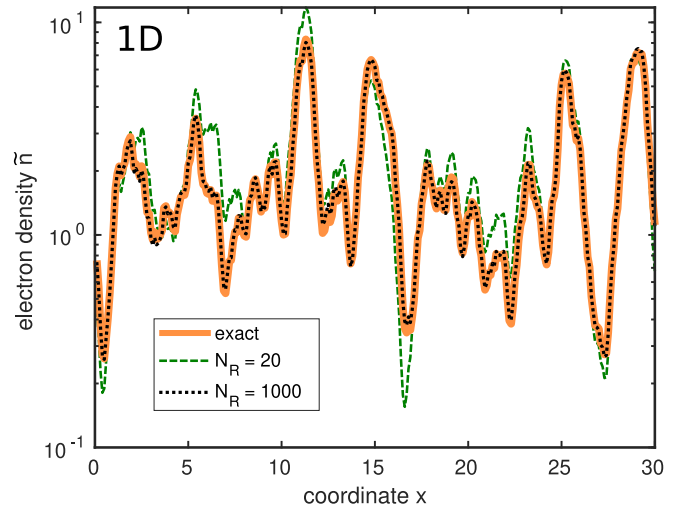


FIG. 1. Reduced electron density $\tilde{n}(x, T) = e^{-\beta\mu} n(x, T)$ as a function of coordinate x in a sample with one-dimensional white-noise potential. Solid orange line: exact density calculated using Eq. (10). Other lines: density calculated by the random-wave-function algorithm with $N_R = 20$ (green dashed line) and $N_R = 1000$ (black dotted line) realizations. Dimensionless units defined in Eqs. (43)–(45) are used. The sample size is equal to 30 dimensionless units, the discretization parameter is $a = 0.1$, the temperature is $T = 1$.

demonstrates the correctness of the estimate (34) for the accuracy of the random-wave-function algorithm.

The only free parameter of the model is the dimensionless temperature T . So far, we tested our algorithm for $T = T_0$ only. Now, we apply it for a variety of temperatures, $0.1T_0 \leq T \leq 10T_0$. The results for the reduced electron density $\tilde{n}(x, T)$ are shown in Fig. 3. Lines represent the exact density calculated by a diagonalization of the Hamiltonian and applying

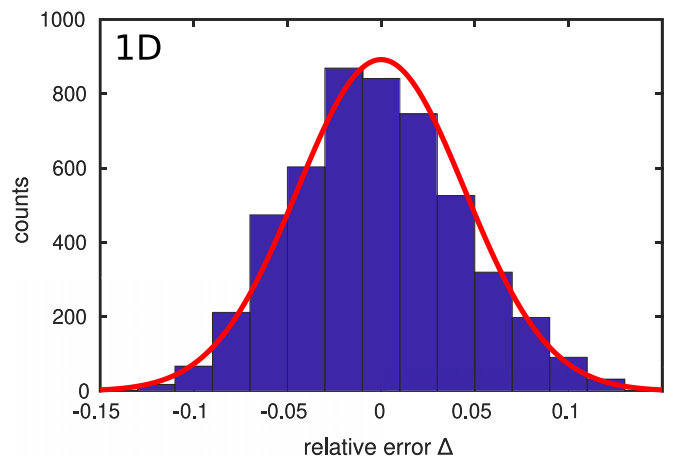


FIG. 2. Distribution of the relative error Δ of the random-wave-function algorithm with $N_R = 1000$ in a sample with a one-dimensional white-noise potential. The quantity Δ is defined in Eq. (33). Blue bars: histogram of the numerically obtained distribution. Red line: Gaussian distribution with expectation value zero and variance $2/N_R$. Parameters are the same as in Fig. 1, except for the sample size that equals 500 dimensionless units.

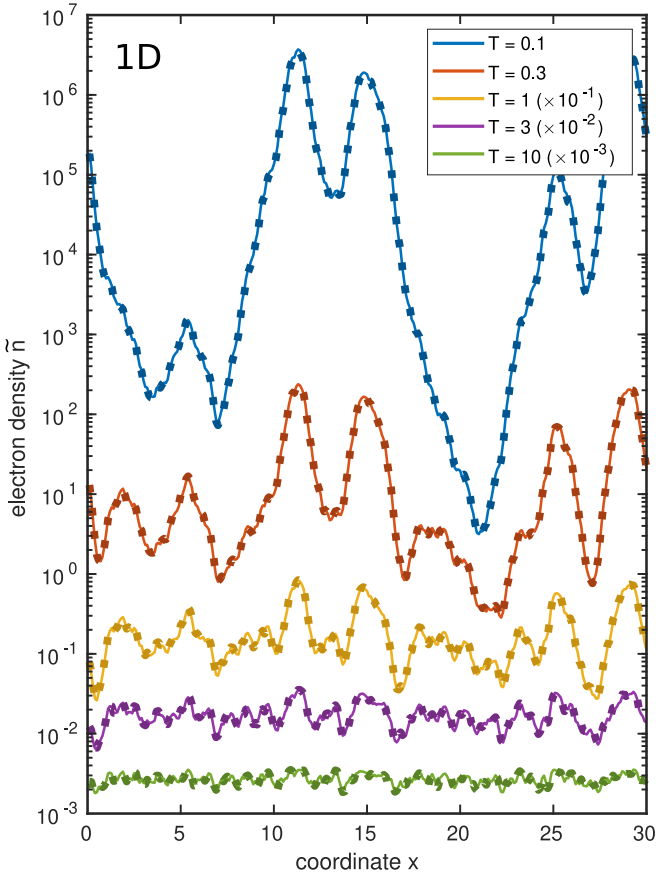


FIG. 3. Comparison between exact (solid lines) and approximate (symbols) reduced electron density $\tilde{n}(x, T) = e^{-\beta\mu}n(x, T)$ in a one-dimensional white-noise potential at different temperatures T and $N_R = 1000$ iterations. All other parameters are the same as in Fig. 1, except for the temperature. For clarity, the lowest three curves are scaled down by a multiplication by 10^{-3} , 10^{-2} , and 10^{-1} , as indicated in the legend.

Eq. (10). Dotted lines are obtained by the random-wave-function algorithm with $N_R = 1000$ independent realizations. Just as in Fig. 1, we see that the algorithm enables a very accurate calculation of the electron density. The algorithm is thus seen to work for a broad range of temperatures.

3. Two- and three-dimensional cases

We perform similar numerical studies for 2D and 3D samples of a random white-noise potential. For the sake of comparison with the exact electron density, we consider rather small samples, with the number of grid nodes L less than 10000. This permits a complete numerical diagonalization of the Hamiltonian to obtain the exact value of the electron density via Eqs. (9) and (10) for reference. The size of the 2D sample is chosen to be 5×5 dimensionless units ($L = 2500$), and the size of the 3D sample is chosen to be $2 \times 2 \times 2$ dimensionless units ($L = 8000$), with grid period $a = 0.1$.

For the 2D sample, profiles of the reduced electron density $\tilde{n}(x, y, T)$ along the x axis at several values of y are shown in Fig. 4. Similarly, the x profiles of the reduced density $\tilde{n}(x, y, z, T)$ in the 3D sample at fixed values of y and z are shown in Fig. 5. The color scheme in these figures is the same

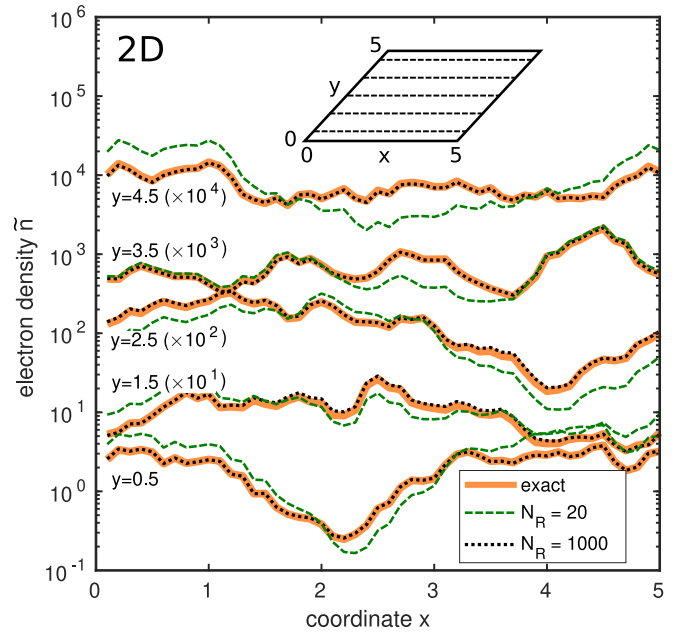


FIG. 4. Reduced electron density $\tilde{n}(x, y, T)$ in a two-dimensional sample with white-noise potential. We compare the exact reduced density (solid orange line) with the approximate reduced density obtained from the random-wave-function algorithm (dashed green line for $N_R = 20$ and dotted black line for $N_R = 1000$). Profiles along the x axis with different values of coordinate y are shown (see inset). The sample size is 5×5 dimensionless units, the discretization grid parameter is $a = 0.1$, the temperature is $T = 1$. Periodic boundary conditions apply. For clarity, profiles are multiplied by different coefficients, as indicated in the plot.

as in Fig. 1. The exact density $\tilde{n}(\mathbf{r}, T)$ is plotted as an orange solid line, and the densities obtained via the random-wave-function algorithm with $N_R = 20$ and $N_R = 1000$ by a green dashed line and by a black dotted line, respectively.

The question might arise on why the data in Fig. 4 look qualitatively different to those in Fig. 5. While the dashed green line in Fig. 4 (2D case) appears to fluctuate around the exact results, it appears to be shifted upwards by a close to constant amount at each point in Fig. 5 (3D case). This qualitative difference is due to the different sizes of the samples simulated in 2D case and in 3D case.

Figures 4 and 5 show that the random-wave-function algorithm provides qualitatively correct results already for a small number of iterations, $N_R = 20$. With $N_R = 1000$ iterations, we can reproduce the electron density very accurately. Hence, our method to determine the density for a nondegenerate, noninteracting electron gas is seen to work for 1D, 2D, and 3D random potentials. The RWF algorithm permits us to obtain the electron density in much larger samples where a straightforward full diagonalization of the Hamiltonian is not longer feasible.

III. EFFECTIVE POTENTIAL

In this section we relate the electron density $n(\mathbf{r}, T)$ to a (quasi)classical, temperature-dependent effective potential $W(\mathbf{r}, T)$ for two reasons. First, the random-wave-function

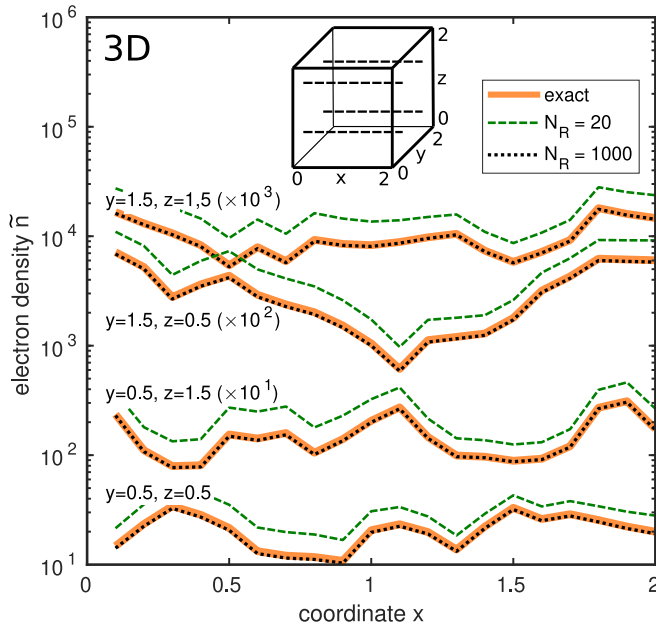


FIG. 5. Reduced electron density $\tilde{n}(x, y, z, T)$ in a three-dimensional sample with white-noise potential. Compared are the exact density (solid orange line) with that obtained by the random-wave-function algorithm (dashed green line for $N_R = 20$ and dotted black line for $N_R = 1000$). Profiles along the x axis with different values of coordinates y and z are shown (see inset). Sample size is $2 \times 2 \times 2$ dimensionless units, the discretization grid parameter is $a = 0.1$, the temperature is $T = 1$. Periodic boundary conditions apply. For clarity, profiles are multiplied by different coefficients, as indicated in the plot.

algorithm requires matrix multiplications with (sparse) $L \times L$ matrices where L is the number of grid points of the sample, and we are interested to find a numerical method that scales more favorably in the system size. Second, $W(\mathbf{r}, T)$ visualizes the potential landscape in which classical particles would move so that concepts like percolation theory can be applied.

A. Quasiclassical effective potential

We start from the well-known expression for the electron density $n(\mathbf{r}, T)$ of a nondegenerate electron gas, e.g., in the conduction band of a semiconductor,

$$n(T) = N_c \exp\left(\frac{\mu - V}{k_B T}\right) \quad (\text{constant potential}), \quad (46)$$

where V is the energy of the conduction band edge, i.e., the electrons' potential energy, and N_c is the effective density of states,

$$N_c = 2 \left(\frac{m k_B T}{2\pi \hbar^2} \right)^{d/2}, \quad (47)$$

in d dimensions. The relation (46) remains applicable also in the case of a coordinate-dependent potential $V(\mathbf{r})$ if the potential is smooth on the scale of the de-Broglie wavelength,

$$n(\mathbf{r}, T) = N_c \exp\left[\frac{\mu - V(\mathbf{r})}{k_B T}\right] \quad (\text{smooth potential}). \quad (48)$$

In other words, electrons near the position \mathbf{r} feel only the local value $V(\mathbf{r})$ of the potential. This approximation corresponds to the quasiclassical description of electron motion in a smooth potential $V(\mathbf{r})$. However, Eq. (48) cannot be applied when the potential fluctuates significantly on length scales less or equal to the de-Broglie wavelength. Since the particles are strongly scattered by the potential, the quasiclassical picture of a compact wave packet breaks down.

As a result of the quantum-mechanical treatment, the electron density at some point \mathbf{r} is affected by the potential not only at \mathbf{r} but also in some extended vicinity. Therefore, the electron density is a much smoother function of coordinates than the potential. In this sense one might argue that the electron gas experiences a “smoothed” potential. Therefore, instead of Eq. (48), one might expect that the electron density obeys

$$n(\mathbf{r}, T) = N_c \exp\left[\frac{\mu - W(\mathbf{r}, T)}{k_B T}\right], \quad (49)$$

where $W(\mathbf{r}, T)$ is the quasiclassical effective potential in the case of a strongly fluctuating potential. This potential is obtained from the actual potential $V(\mathbf{r})$ by some appropriate operation of “smoothing.”

We will consider Eq. (49) as the very *definition* of the quasiclassical effective potential $W(\mathbf{r}, T)$. Hence,

$$W(\mathbf{r}, T) \stackrel{\text{def}}{=} \mu(T) - k_B T \ln \frac{n(\mathbf{r}, T)}{N_c}. \quad (50)$$

It is important to note that the effective potential $W(\mathbf{r}, T)$ depends on temperature. This temperature dependence is demonstrated numerically in Sec. III C for the example of a white-noise potential. For this reason, the effective potential introduced here differs from that of the Localization-Landscape Theory where the effective potential $W_{\text{LLT}}(\mathbf{r})$ is independent of T .

B. Linear low-pass filter

To simplify the notation, in this subsection we drop the temperature-dependence of all quantities. Let us consider the response $\delta n(\mathbf{r})$ of the electron gas density to a variation $\delta V(\mathbf{r}')$ of the potential. To first order in δV ,

$$\delta n(\mathbf{r}) = \int d\mathbf{r}' \Gamma_n(\mathbf{r}, \mathbf{r}') \delta V(\mathbf{r}') + \mathcal{O}(\delta V^2), \quad (51)$$

where the linear-response function $\Gamma_n(\mathbf{r}, \mathbf{r}')$ can be defined as a functional derivative,

$$\Gamma_n(\mathbf{r}, \mathbf{r}') = \frac{\delta n(\mathbf{r})}{\delta V(\mathbf{r}')}. \quad (52)$$

Likewise, one can define a linear-response function Γ_W for the effective potential W ,

$$\delta W(\mathbf{r}) = \int d\mathbf{r}' \Gamma_W(\mathbf{r}, \mathbf{r}') \delta V(\mathbf{r}') + \mathcal{O}(\delta V^2), \quad (53)$$

or, equivalently, as a functional derivative,

$$\Gamma_W(\mathbf{r}, \mathbf{r}') = \frac{\delta W(\mathbf{r})}{\delta V(\mathbf{r}')}. \quad (54)$$

The relation between the response functions Γ_n and Γ_W can be readily found using the chain rule and Eq. (50),

$$\Gamma_W(\mathbf{r}, \mathbf{r}') = \frac{dW(\mathbf{r})}{dn(\mathbf{r})} \frac{\delta n(\mathbf{r})}{\delta V(\mathbf{r}')} = -\frac{k_B T}{n(\mathbf{r})} \Gamma_n(\mathbf{r}, \mathbf{r}'). \quad (55)$$

In Sec. III D we show how to evaluate these response functions with the help of perturbation theory.

The function Γ_W has a remarkable property: it is normalized to unity,

$$\int d\mathbf{r}' \Gamma_W(\mathbf{r}, \mathbf{r}') = 1. \quad (56)$$

To see this, we insert a coordinate-independent variation $\delta V(\mathbf{r}) = \text{const} = \delta V$ into Eq. (53) and obtain

$$\delta W(\mathbf{r}) = \delta V \int d\mathbf{r}' \Gamma_W(\mathbf{r}, \mathbf{r}') + \mathcal{O}(\delta V^2). \quad (57)$$

However, adding a constant δV to the potential gives rise to the same shift of all electron energy levels ϵ_i . The electron density therefore is changed by a factor of $\exp[-\delta V/(k_B T)]$. According to definition (50), the effective potential $W(\mathbf{r})$ acquires the constant shift

$$\delta W(\mathbf{r}) = \delta V. \quad (58)$$

The normalization condition (56) then follows from the comparison of Eqs. (57) and (58).

Since the function Γ_W is properly normalized, it may play the role of a filter function that produces the effective potential $W(\mathbf{r})$ from the actual potential $V(\mathbf{r})$ by the operation of convolution. However, a filter function must depend on the difference $\mathbf{r} - \mathbf{r}'$ only, not on \mathbf{r} and \mathbf{r}' separately. For a random potential $V(\mathbf{r})$ this is not the case because the right-hand side of Eq. (54) depends on this potential which breaks translational invariance. Nevertheless, in a statistical sense we may argue that the response function $\Gamma_W(\mathbf{r}, \mathbf{r}')$ that applies for a typical realization of the disorder potential can be approximated by some translationally invariant function,

$$\Gamma_W(\mathbf{r}, \mathbf{r}') = \Gamma(\mathbf{r} - \mathbf{r}'), \quad (59)$$

or, implying that the system also is isotropic in a statistical sense,

$$\Gamma_W(\mathbf{r}, \mathbf{r}') = \Gamma(|\mathbf{r} - \mathbf{r}'|). \quad (60)$$

Due to translational invariance, the function Γ does not depend on the choice of the realization of the random potential. One can therefore integrate the differential relation (53) between two random realizations $V_1(\mathbf{r})$ and $V_2(\mathbf{r})$ which yields $U_1(\mathbf{r}) = U_2(\mathbf{r})$ where

$$U_i(\mathbf{r}) = W_i(\mathbf{r}) - \int d\mathbf{r}' \Gamma(|\mathbf{r} - \mathbf{r}'|) V_i(\mathbf{r}'), \quad (61)$$

that relates the effective potentials W_1 and W_2 to the actual potentials V_1 and V_2 , respectively. Consequently, $U_i(\mathbf{r}) \equiv C$, whereby the constant C does not depend on the choice of the realization. In sum, the hypothesis (60) gives rise to the following relation between the actual potential $V(\mathbf{r})$ and the effective potential $W(\mathbf{r})$,

$$W(\mathbf{r}) = \int d\mathbf{r}' \Gamma(|\mathbf{r} - \mathbf{r}'|) V(\mathbf{r}') + C. \quad (62)$$

In words, *the effective potential W is a convolution of the real potential V with the filter function Γ , plus some constant C* . Note that the convolution with Γ is nothing else but passing the original potential through the linear low-pass filter defined by Γ . For this reason, the effective potential $W(\mathbf{r})$ becomes much smoother than the original potential $V(\mathbf{r})$. Since the effective potential depends also on the temperature, the filter function Γ and C are temperature-dependent as well, $\Gamma \equiv \Gamma(|\mathbf{r} - \mathbf{r}'|, T)$ and $C \equiv C(T)$.

In Sec. III C, we test Eq. (62) numerically for the case of a white-noise random potential, and ensure that it works surprisingly well, except for very low temperatures. In Sec. III D, we show that the filter function Γ can approximately be reduced to some universal function Γ_{uni} by the simple scaling relation

$$\Gamma(r) \approx \tilde{\lambda}^{-d} \Gamma_{\text{uni}}(r/\tilde{\lambda}), \quad (63)$$

where d is the spatial dimension, and $\tilde{\lambda}$ is the reduced de-Broglie wavelength of a charge carrier of mass m and kinetic energy $k_B T$,

$$\tilde{\lambda} = \frac{\hbar}{\sqrt{2mk_B T}}, \quad (64)$$

which is the thermal wave length up to a numerical factor.

C. Numerical study of a white-noise potential

In our numerical study of a white-noise potential, we employ the model of white noise and the dimensionless system of units described in Sec. II D, $\hbar = k_B = m = S = 1$. The discretization parameter a , the distance between grid nodes, is chosen to be $a = 0.1$. Periodic boundary conditions apply. We consider a collection of 100 random samples of length 500 in 1D, a collection of 20 samples of size 10×10 in 2D, and a collection of 10 samples of size $10 \times 10 \times 10$ in 3D. For each of these samples, we calculate the reduced electron density $\tilde{n}(\mathbf{r}, T)$. In 1D and 2D, we use the definition of $\tilde{n}(\mathbf{r}, T)$, Eq. (10), in which we employ the eigenfunctions $\varphi_i(\mathbf{r})$ and eigenvalues ϵ_i from the numerical diagonalization of the Hamiltonian matrix. In 3D, the Hamiltonian matrix is too large ($10^6 \times 10^6$) for an exact numerical diagonalization so that we derive $\tilde{n}(\mathbf{r}, T)$ from the random-wave-function algorithm described in Sec. II C where we choose $N_R \approx 1000\sqrt{T}$ realizations so that the accuracy for $\tilde{n}(\mathbf{r}, T)$ is about 5% relative to the amplitude of spatial fluctuations. The temperature-dependent effective potential $W(\mathbf{r}, T)$ is then calculated from the reduced electron density as

$$W(\mathbf{r}, T) = -k_B T \ln \frac{\tilde{n}(\mathbf{r}, T)}{N_c}, \quad (65)$$

according to the definition (50). Since we have a collection of random potentials $V_R(\mathbf{r})$ and effective potentials $W_R(\mathbf{r}, T)$, we can test the validity of the filter function approach, which is expressed mathematically by Eq. (62).

Before we apply the filter function approach, some preliminary steps must be carried out. First, we need to determine the value of the parameter C in Eq. (62). Second, it is necessary to estimate the characteristic range of the filter function $\Gamma(r)$. Third, we have to determine the optimal shape of this filter function.

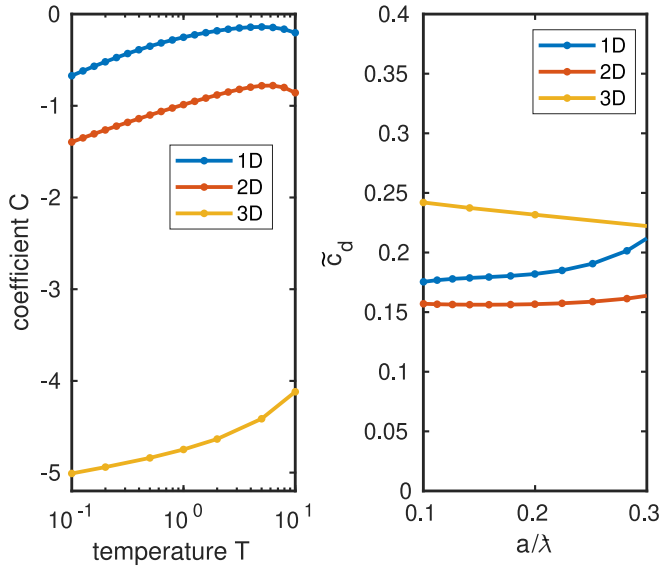


FIG. 6. Left panel: parameter $C(T)$ as function of the temperature T for systems with white-noise disorder in one, two, and three dimensions. The effective potential is defined by Eq. (50). The parameter C is the average of the effective potential, $C = \langle W_R \rangle_R$ and used in Eq. (62). Dimensionless units ($\hbar = k_B = m = S = 1$) introduced in Sec. IID are used. Grid spacing $a = 0.1$. Right panel: parameter function $\tilde{c}_d(a, T)$ defined in Eq. (68) as a function of a/λ . The limit $a/\lambda \rightarrow 0$ defines the constants c_d .

1. Constant parameter

To evaluate the parameter C , we note that the mean value of the integral in Eq. (62) is equal to the mean value of V because of the normalization property (56) of the filter function. Therefore, when we take the mean values of both sides of Eq. (62), we obtain

$$C = \langle W_R \rangle_R - \langle V_R \rangle_R, \quad (66)$$

where the brackets denote the average value over the collection of samples. In the model used, the mean value of the potential V_R is equal to zero. Hence, $C = \langle W_R \rangle_R$. The resulting values of C in the temperature range $0.1 \leq T \leq 10$ are plotted in Fig. 6, left part. It is worth noting that the constant C depends on the grid spacing a . The data in Fig. 6 are calculated for $a = 0.1$.

To extend the result to arbitrary values of a , we employ the following scaling argument that is corroborated in Appendix B. The effective potential $W(\mathbf{r}, T)$ results from the random potential $V(\mathbf{r})$ according to the linear mapping given in Eq. (62). The contribution proportional to $V(\mathbf{r})$ is obtained from first-order perturbation theory, as explained in Sec. IIID. Second-order perturbation contributes to C , after averaging over various realizations of potential $V_R(\mathbf{r})$. Consequently, C is proportional to the potential squared and hence to the parameter S determined in Eq. (38). The proportionality coefficient between C and S then follows from the physical dimensions of these quantities. While C is energy, S is energy squared times volume, as evident from Eq. (39). Therefore, $C_d(a, T)/S = F_d(a/\lambda)/(k_B T \lambda^d)$, where the thermal de-Broglie wavelength λ is determined from Eq. (64),

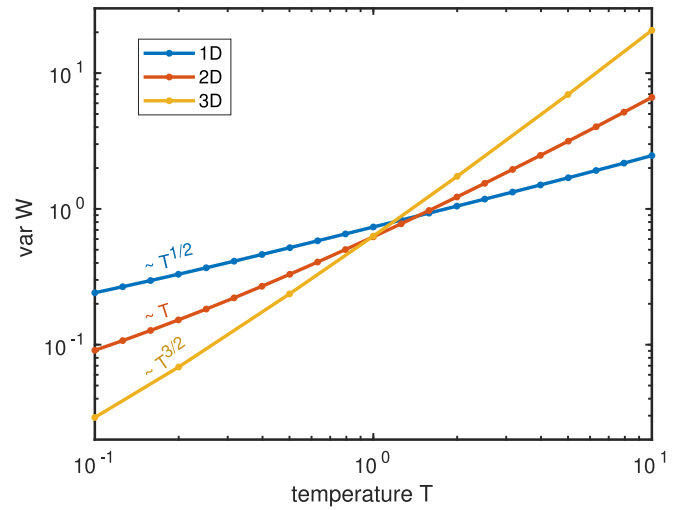


FIG. 7. Variance of the effective potential $W_R(T)$, $\text{var } W_R = \langle W_R^2 \rangle_R - \langle W_R \rangle_R^2$, as function of the temperature T for systems with white-noise disorder in one, two, and three dimensions. Dimensionless units ($\hbar = k_B = m = S = 1$) introduced in Sec. IID are used. Grid spacing $a = 0.1$.

and the function $F_d(x)$ carries no units. It depends on the dimension d and on the ratio a/λ .

As shown in Appendix B, in the limit $x \rightarrow 0$, i.e., $a \ll \lambda$, we have $F_d(x) = c_d f_d(x)$ with $f_1(x) = -1$, $f_2(x) = \ln(0.30x)$, and $f_3(x) = -1/x$. Therefore,

$$C_d(a, T) = S \frac{c_d f_d(a/\lambda)}{k_B T \lambda^d}, \quad (67)$$

where c_d are numerical factors. To determine their values, we plot

$$\tilde{c}_d(a, T) = \frac{C_d(a, T) k_B T \lambda^d}{S f_d(a/\lambda)} \quad (68)$$

in Fig. 6, right panel. The figure proves the scaling behavior expressed in Eq. (67) and permits us to read off $c_1 = 0.183$, $c_2 = 1/(2\pi) \approx 0.159$, and $c_3 = 0.255$ for the constants in $d = 1, 2, 3$ dimensions.

2. Characteristic scale

To determine the characteristic scale ℓ_Γ of the filter function Γ , we repeat the considerations from Sec. IID and get the following estimate similar to Eq. (41),

$$\text{var } W_R \simeq \frac{S}{\ell_\Gamma^d}, \quad (69)$$

where the symbol “var” denotes the variance, the square of the standard deviation. We show the variance of W for different temperatures and spatial dimensions in Fig. 7. Our numerical data clearly demonstrate that $\text{var } W \sim T^{d/2}$. Inserting this dependence into Eq. (69), we see that ℓ_Γ scales with temperature T as $\ell_\Gamma \simeq 1/\sqrt{T}$. This temperature dependence is the same as that of the thermal wavelength λ , see Eq. (64). Specifically, $\lambda = 1/\sqrt{2T}$ in dimensionless units. Therefore,

$$\ell_\Gamma \simeq \lambda \propto T^{-1/2} \quad (70)$$

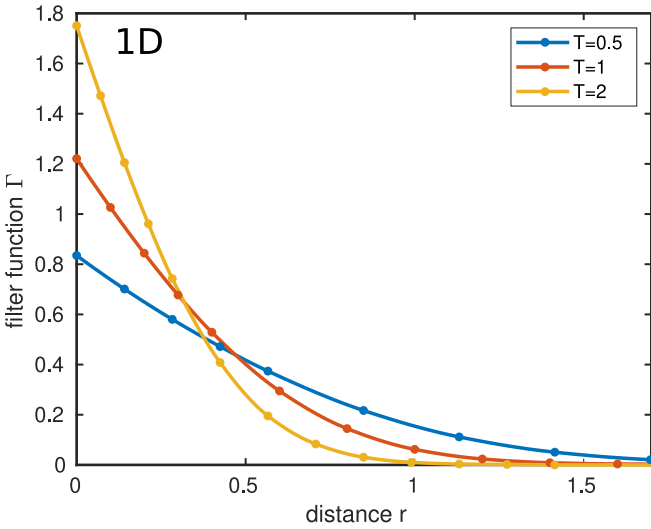


FIG. 8. Filter functions $\Gamma(r)$ at different temperatures T in 1D systems with white-noise potential as obtained from the optimization procedure. The dots indicate values of $\Gamma(r)$ that serve as fitting parameters. Dimensionless units ($\hbar = k_B = m = S = 1$) introduced in Sec. IID are used.

holds. The characteristic scale is simply the de-Broglie wave length.

3. Shape of the low-pass filter

To obtain the optimal shape of the low-pass filter $\Gamma(r)$, we use the following variational scheme. As a set of fitting parameters, we choose Γ at $N \simeq 10$ points $r_0 = 0, r_1, \dots, r_N = 2/\sqrt{T}$. The whole function $\Gamma(r)$ is restored from the values $\Gamma(r_0), \dots, \Gamma(r_N)$ using a cubic spline interpolation. Two restrictions are imposed to the fitting parameters: (i) $\Gamma(r_N)$ is fixed to zero and, (ii) the normalization integral $\int \Gamma(|\mathbf{r}|) d\mathbf{r}$ is fixed to unity. The values $\Gamma(r_0), \dots, \Gamma(r_{N-1})$ are varied until the minimum of the relative error of the effective potential

$$\mathfrak{E}[\Gamma] = \frac{\sqrt{\langle (W_\Gamma(\mathbf{r}) - W)^2 \rangle}}{\sqrt{\text{var } W}} \quad (71)$$

is reached. Here, W is the effective potential calculated from the electron density using Eq. (65), and W_Γ is calculated from the potential V and the filter function Γ using Eq. (62). Here, the angular brackets imply spatial integration.

Using this optimization procedure, we obtain the filter function $\Gamma(\mathbf{r}, T)$ in the temperature range $0.1 \leq T \leq 10$ for 1D, 2D, and 3D white-noise potentials. Examples of 1D filter functions for three different temperatures are shown in Fig. 8. It is seen that the width of the filter function narrows with temperature, in agreement with Eq. (70). However, the shape of the filter function remains fairly unchanged with varying the temperature. These properties of the filter function suggest a universal filter function Ansatz, see Eq. (63).

In Fig. 9, we show an example of an effective potential $W_R(x, T)$ in 1D at different temperatures (solid orange lines), along with the estimates obtained by the filter-function approach, Eq. (62) (dashed blue lines). The agreement is quite good in the whole temperature range $T \gtrsim 0.2$. At high enough

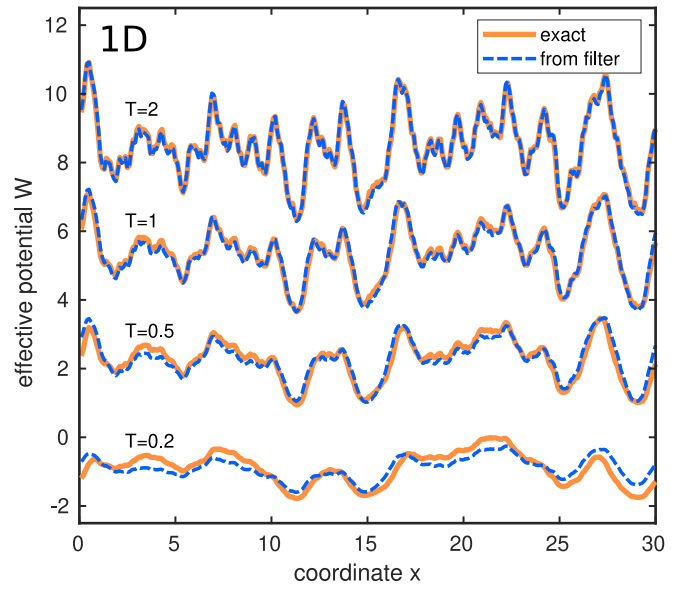


FIG. 9. Comparison between the exact effective potential $W_R(x)$ (solid orange lines) and the filtered potential, see Eq. (62) (dashed blue lines) for a one-dimensional sample with white-noise potential. Filter functions at different temperatures T are obtained by the optimization procedure. Dimensionless units ($\hbar = k_B = m = S = 1$) are used. The sample size is equal to 30 dimensionless units, the discretization parameter is $a = 0.1$. For clarity, curves for $T = 0.5, T = 1$, and $T = 2$ are shifted upwards by 3, 6, and 9 units, respectively.

temperatures, $T \geq 1$, the filter-function approach reproduces the effective potential almost perfectly.

To quantify the accuracy of our approach, we calculate the relative error \mathfrak{E} of the effective potential obtained from by Eq. (71) for different temperatures and spatial dimensions. The results are shown in Fig. 10 by circles. It is seen that the relative error decreases with temperature. In the low-temperature limit, the electron density is dominated by contributions of rare low-energy eigenstates. Therefore, the shape of the electron density distribution $n(\mathbf{r}, T)$ reproduces the probability distributions $|\varphi_i(\mathbf{r})|^2$ of individual eigenstates $\varphi_i(\mathbf{r})$. For this reason, the electron density distribution at very low temperatures requires the solution of the Schrödinger equation, and the filter-function approach becomes less reliable. However, for high temperatures the role of the fluctuating potential becomes negligible, the system under study acquires translational and rotational symmetry. For high temperatures, the validity of Eq. (62) for the filter-function approach is guaranteed because it follows from the universal relation (53), as explained in Sec. III B.

D. Universal filter function

As seen in Sec. III C, the low-pass filter representation of the effective potential $W(\mathbf{r}, T)$ becomes more accurate for higher temperatures. Therefore, it is reasonable to search for a universal filter function in the limit of infinitely high temperature. This limit is characterized by neglecting the random potential altogether. Indeed, the high-temperature limit with a constant strength of the random potential is equivalent to the limit of infinitely small strength of the potential at constant

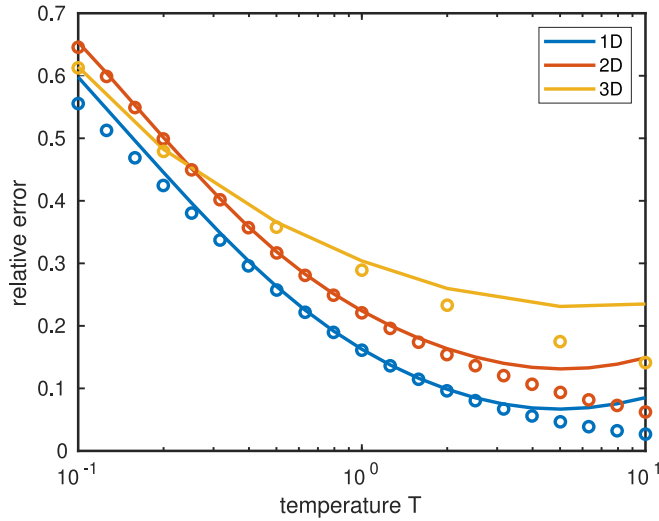


FIG. 10. Relative error \mathcal{E} of the effective potential W obtained from convolution of the potential with the filter function, Eq. (62), at different temperatures T . Circles are related to the filter function obtained from the optimization procedure, lines correspond to the universal filter function considered in Sec. III D. The values of relative error \mathcal{E} are obtained from Eq. (71). Dimensionless units ($\hbar = k_B = m = S = 1$) are used. Discretization parameter $a = 0.1$.

temperature. For this reason, we develop the ULF function in the case of zero potential where the single-electron Hamiltonian \hat{H} reduces to the kinetic energy operator \hat{T} .

In this subsection, we first obtain an expression for the response function $\Gamma_n(\mathbf{r}, \mathbf{r}')$ in terms of the matrix elements of exponents of the Hamiltonian. This will be done in first-order perturbation theory. Then, we consider the case of zero potential, $\hat{H} = \hat{T}$, and find analytical expressions for the response functions Γ_n and Γ_w . The latter plays the role of the filter function. Finally, we determine an expression for the universal dimensionless filter function Γ_{uni} . We numerically test its accuracy at finite temperatures and disorder strengths.

1. Linear response

We start from expressions (9) and (10) that define the electron density $n(\mathbf{r}, T)$ in a noninteracting, nondegenerate electron gas. They can be rewritten in operator notation as

$$n(\mathbf{r}, T) = 2e^{\beta\mu} \langle \mathbf{r} | e^{-\beta\hat{H}} | \mathbf{r} \rangle, \quad (72)$$

where \hat{H} is the single-electron Hamiltonian, and the position-space states $|\mathbf{r}\rangle$ are normalized such that

$$\langle \mathbf{r} | \mathbf{r}' \rangle = \delta(\mathbf{r} - \mathbf{r}'). \quad (73)$$

We are interested in the variation $\delta n(\mathbf{r})$ of the electron density in linear response to a small variation $\delta V(\mathbf{r})$ of the potential. The potential variation can be represented as a small addition $\delta\hat{V}$ to the Hamiltonian,

$$\delta\hat{V} = \int d\mathbf{r}' \delta V(\mathbf{r}') |\mathbf{r}'\rangle \langle \mathbf{r}'|. \quad (74)$$

Therefore,

$$\delta n(\mathbf{r}, T) = 2e^{\beta\mu} \langle \mathbf{r} | [e^{-\beta(\hat{H} + \delta\hat{V})} - e^{-\beta\hat{H}}] | \mathbf{r} \rangle. \quad (75)$$

The difference in square brackets can be evaluated via first-order perturbation theory. Neglecting higher-order infinitesimals we find

$$e^{-\beta(\hat{H} + \delta\hat{V})} - e^{-\beta\hat{H}} = - \int_0^\beta d\xi e^{-\xi\hat{H}} \delta\hat{V} e^{-(\beta-\xi)\hat{H}}. \quad (76)$$

Inserting Eqs. (74) and (76) into Eq. (75), we obtain

$$\begin{aligned} \delta n(\mathbf{r}, T) = & -2e^{\beta\mu} \int_0^\beta d\xi \int d\mathbf{r}' \langle \mathbf{r} | e^{-\xi\hat{H}} | \mathbf{r}' \rangle \\ & \times \delta V(\mathbf{r}') \langle \mathbf{r}' | e^{-(\beta-\xi)\hat{H}} | \mathbf{r} \rangle. \end{aligned} \quad (77)$$

A comparison between Eq. (77) and Eq. (51) provides the following expression for the linear response function $\Gamma_n(\mathbf{r}, \mathbf{r}', T)$:

$$\Gamma_n(\mathbf{r}, \mathbf{r}', T) = -2e^{\beta\mu} \int_0^\beta d\xi \langle \mathbf{r} | e^{-\xi\hat{H}} | \mathbf{r}' \rangle \langle \mathbf{r}' | e^{-(\beta-\xi)\hat{H}} | \mathbf{r} \rangle, \quad (78)$$

within first-order perturbation theory.

2. Linear response for free electrons

Now we turn to the particular case of free electrons, where the Hamiltonian reduces to the kinetic energy operator \hat{T} ,

$$\hat{H} = \hat{T} = \sum_{\mathbf{k}} \frac{\hbar^2 |\mathbf{k}|^2}{2m} |\mathbf{k}\rangle \langle \mathbf{k}|, \quad (79)$$

where the wave-number states $|\mathbf{k}\rangle$ are related to the position-space states $|\mathbf{r}\rangle$ as

$$\langle \mathbf{r} | \mathbf{k} \rangle = \frac{e^{i\mathbf{k}\cdot\mathbf{r}}}{\sqrt{\Omega}}. \quad (80)$$

We insert Eqs. (79) and (80) into Eq. (78) to find

$$\begin{aligned} \Gamma_n(\mathbf{r}, \mathbf{r}', T) = & -\frac{2e^{\beta\mu}}{\Omega^2} \sum_{\mathbf{k}, \mathbf{k}'} \int_0^\beta d\xi F(\xi, \mathbf{k}, \mathbf{k}'), \\ F(\xi, \mathbf{k}, \mathbf{k}') = & \exp \left[\frac{\hbar^2 (\xi - \beta) |\mathbf{k}'|^2 - \xi |\mathbf{k}|^2}{2m} \right] e^{i(\mathbf{k} - \mathbf{k}') \cdot (\mathbf{r} - \mathbf{r}')}. \end{aligned} \quad (81)$$

We perform the integral over ξ , replace the sums over \mathbf{k} by integrations over $d\mathbf{k} \times \Omega / (2\pi)^d$, and discard the imaginary part to arrive at an analytical expression for the response function,

$$\Gamma_n(\mathbf{r}, \mathbf{r}', T) = \frac{4me^{\beta\mu}}{\hbar^2 (2\pi)^{2d}} \iint d\mathbf{k} d\mathbf{k}' G(\mathbf{k}, \mathbf{k}'), \quad (82)$$

$$\begin{aligned} G(\mathbf{k}, \mathbf{k}') = & \left[\exp \left(-\frac{\beta\hbar^2 |\mathbf{k}|^2}{2m} \right) - \exp \left(-\frac{\beta\hbar^2 |\mathbf{k}'|^2}{2m} \right) \right] \\ & \times \frac{\cos [(\mathbf{k} - \mathbf{k}') \cdot (\mathbf{r} - \mathbf{r}')] }{|\mathbf{k}|^2 - |\mathbf{k}'|^2}, \end{aligned} \quad (83)$$

where the integrand at $|\mathbf{k}| = |\mathbf{k}'|$ is to be resolved by L'Hôpital's rule.

The response function $\Gamma_w(\mathbf{r}, \mathbf{r}', T)$ for the effective potential can be calculated from Eq. (55). In the absence of an external potential, we use Eq. (46) for the electron density

$n(T)$ in a constant potential $V = 0$. As a result, we obtain the function

$$\Gamma_W(\mathbf{r}, \mathbf{r}') = \frac{\lambda^d}{2^d \pi^{3d/2}} \iint d\mathbf{k} d\mathbf{k}' \frac{e^{-|\lambda\mathbf{k}|^2} - e^{-|\lambda\mathbf{k}'|^2}}{|\lambda\mathbf{k}'|^2 - |\lambda\mathbf{k}|^2} \times \cos[(\mathbf{k} - \mathbf{k}') \cdot (\mathbf{r} - \mathbf{r}')], \quad (84)$$

where we employ de-Broglie wavelength λ from Eq. (64).

Equation (84) provides the filter function $\Gamma(|\mathbf{r} - \mathbf{r}'|) \equiv \Gamma_W(\mathbf{r}, \mathbf{r}')$, introduced in Eq. (60). After substitutions $\lambda\mathbf{k} = \mathbf{q}$, $\lambda\mathbf{k}' = \mathbf{q}'$, we arrive at Eq. (63) that expresses the temperature-dependent filter function Γ via a universal, dimensionless function Γ_{uni} . This universal function, obtained with the help of Eq. (84), is equal to

$$\Gamma_{\text{uni}}(|\tilde{\mathbf{r}}|) = \frac{1}{2^d \pi^{3d/2}} \iint d\mathbf{q} d\mathbf{q}' (e^{-|\mathbf{q}|^2} - e^{-|\mathbf{q}'|^2}) \times \frac{\cos[(\mathbf{q} - \mathbf{q}') \cdot \tilde{\mathbf{r}}]}{|\mathbf{q}'|^2 - |\mathbf{q}|^2}, \quad (85)$$

where $\tilde{\mathbf{r}} = \mathbf{r}/\lambda$ is a dimensionless radius vector.

This expression can be simplified by means of Fourier transform. The Fourier image $\hat{\Gamma}_{\text{uni}}(k)$ of the universal filter function is defined as

$$\hat{\Gamma}_{\text{uni}}(|\mathbf{k}|) = \int d\mathbf{r} \Gamma_{\text{uni}}(|\mathbf{r}|) e^{i\mathbf{k} \cdot \mathbf{r}}. \quad (86)$$

The substitution of Eq. (85) into Eq. (86) gives rise to the simple result

$$\hat{\Gamma}_{\text{uni}}(k) = \frac{\sqrt{\pi}}{k} e^{-k^2/4} \text{erfi}(k/2), \quad (87)$$

where erfi is the imaginary error function,

$$\text{erfi}(\xi) = -i \text{erf}(i\xi) = \frac{2}{\sqrt{\pi}} \int_0^\xi e^{t^2} dt. \quad (88)$$

Expression (87) resembles the filter function, which has been used by Steinerberger [35] to construct the effective potential from the initial random one. Note that the function $\hat{\Gamma}_{\text{uni}}(k)$ does not depend on the spatial dimension. The Fourier image $\hat{\Gamma}(k)$ of the temperature-dependent filter function $\Gamma(r)$ is obtained from Eq. (63),

$$\hat{\Gamma}(k) \approx \hat{\Gamma}_{\text{uni}}(\lambda k). \quad (89)$$

In Fig. 11, we compare the filter functions $\Gamma(r)$ obtained by the optimization procedure in Sec. III C with the universal function $\Gamma_{\text{uni}}(r)$. For this purpose, we multiply the temperature-dependent filter functions by λ^d , and plot them versus r/λ . The universal functions, obtained by inverse Fourier transformation of Eq. (87), are shown by thick violet lines. A dimensionless system of units is used, in which $\hbar = k_B = m = S = 1$ and hence $\lambda = 1/\sqrt{2T}$. It is seen that in all dimension the scaled filter functions approximately follow the universal function Γ_{uni} . Therefore, the scaling property (63) of the filter functions is numerically confirmed, and the expression (87) for the universal filter function is validated.

3. Effective potentials using a universal low-pass filter

Using a ULF provides a practical numerical method for the calculation of the electron density distribution $n(\mathbf{r}, T)$ for

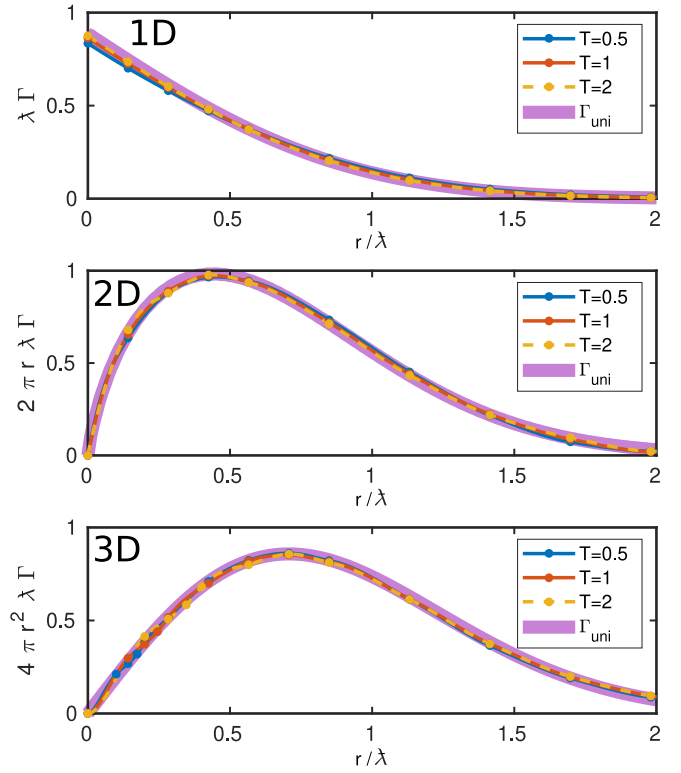


FIG. 11. Radial filter functions $\Gamma_W^{(d)}(r/\lambda)$ ($d = 1, 2, 3$ from top to bottom), obtained from the optimization procedure in Sec. III C, plotted versus r/λ , in comparison with the universal filter function Γ_{uni} (thick violet line). Dimensionless units ($\hbar = k_B = m = S = 1$) are used. $\lambda = 1/\sqrt{2T}$ is the reduced de-Broglie wavelength at kinetic energy equal to T . The discretization parameter is $a = 0.1$.

a given realization of the white-noise potential $V_R(\mathbf{r})$. The method consists of the following simple steps.

(1) Calculate the Fourier image $\hat{V}_R(\mathbf{k})$ of the random potential by means of a fast-Fourier-transform (FFT) algorithm.

(2) Multiply the function $\hat{V}_R(\mathbf{k})$ by $\hat{\Gamma}(|\mathbf{k}|)$, where $\hat{\Gamma}(|\mathbf{k}|)$ is given by Eqs. (64), (87), and (89).

(3) Perform the inverse Fourier transform of the product $\hat{V}(\mathbf{k})\hat{\Gamma}(|\mathbf{k}|)$ by FFT, and add the constant $C(T)$ to the result; see Eq. (67). The output of the third step is the effective potential $W_R(\mathbf{r}, T)$ which follows from Eq. (62) and from the fact that inverse Fourier transform converts a product into a convolution.

(4) Calculate the electron density $n(\mathbf{r}, T)$ from the effective potential $W_R(\mathbf{r}, T)$ using Eq. (49).

Since the numerical effort in FFT scales proportional to $L \ln(L)$, the effective potential $W(\mathbf{r}, T)$ and the particle density $n(\mathbf{r}, T)$ can be calculated for mesoscopically large systems from a microscopic random potential $V(\mathbf{r})$.

4. Numerical tests

Last, we present numerical tests of our method. Figure 10 shows the relative error of the calculated effective potential $W(\mathbf{r}, T)$ with the global filter (lines) in comparison with the same calculation using filter functions obtained numerically by an optimization procedure (circles). It is seen that for a broad range of temperatures, the universal filter function

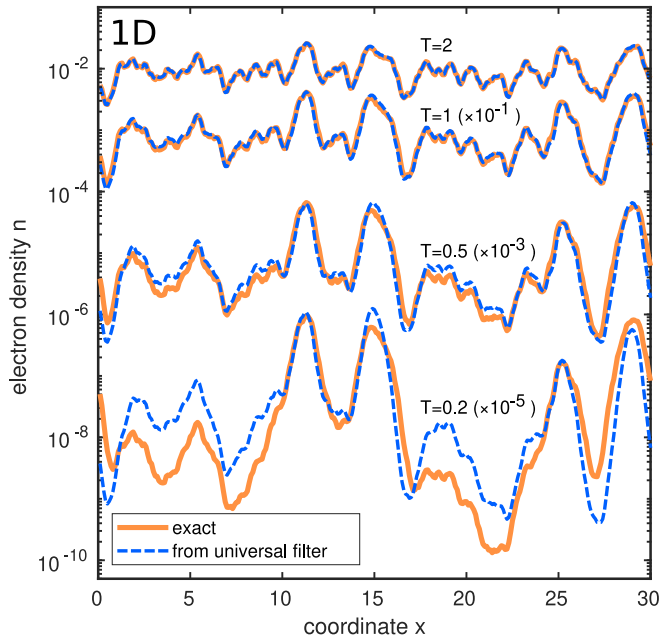


FIG. 12. Electron density $n(x, T)$ in a one-dimensional white-noise potential at different temperatures T : exact (solid orange lines) and ULF (dashed blue lines). The parameters are the same as in Fig. 1, except for the temperature T . For clarity, the curves related to $T = 0.2$, $T = 1$ and $T = 2$ are multiplied by 10^{-4} , 10^2 , and 10^3 , respectively, as indicated in the plot; particle concentration $n = 0.01$.

provides as accurate results as using the numerically optimized one. An exception is the case of very high temperatures, presumably due to discretization errors.

We compare the electron density distributions $n(\mathbf{r}, T)$ obtained by different numerical techniques. Expressions (9), (32), and (49) determine $n(\mathbf{r}, T)$ up to the factor $e^{\beta\mu}$, where $\mu(T)$ is the chemical potential. To remedy this ambiguity, we fix the average electron concentration $n = N/\Omega$ at $n = 0.01$. Here, N is the number of electrons, and Ω is the sample volume. This concentration is much less than N_c which permits us to treat the electron gas as nondegenerate.

Figure 12 clearly demonstrates in 1D that the method is fairly accurate at temperatures $T \geq 0.5$. Here, the temperature is expressed in dimensionless units introduced in Sec. II D. Even for much smaller temperatures, where the electron density $n(x, T)$ fluctuates by several orders of magnitude, the universal-filter approach correctly predicts the positions of maxima and minima of $n(x, T)$.

Figure 13 shows an application for a 2D system with a white-noise potential at $T = 1$. Since we fix the concentration $n = 0.01$ and work with a single particle species, the effect of the constant $C(T)$ can be absorbed in the chemical potential, $\tilde{\mu}(T) \equiv \mu(T) - C(T)$. As can be seen from Fig. 13, the exact result (upper plot) is accurately reproduced by the calculation based on the universal filter function (lower plot).

Figure 14 shows an application for a 3D system with a white-noise potential at $T = 2$. The cross section of $n(x, y, z, T)$ at $z = 0$ is plotted. The upper plot depicts the electron density distribution $n(x, y, z, T)$ obtained by the random-wave-function algorithm with relative accuracy 5%.

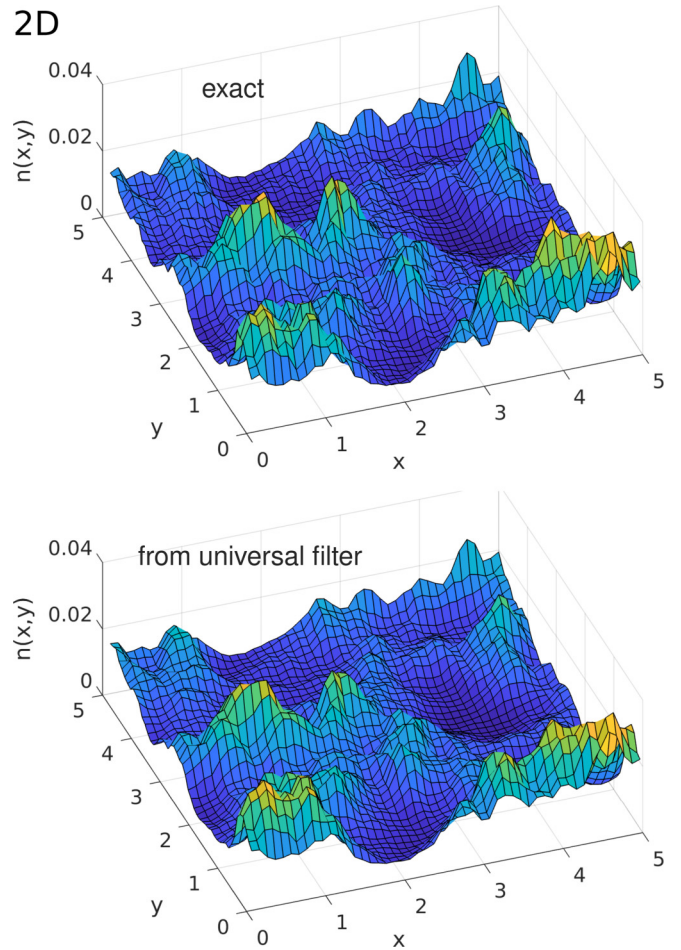


FIG. 13. Comparison between the exact electron density $n(x, y, T)$ (upper part) and that obtained by using the universal filter function (lower part) in a two-dimensional white-noise potential. The sample size is 5×5 dimensionless units, the discretization parameter is $a = 0.1$, the temperature is $T = 1$, the particle concentration is $n = 0.01$. Periodic boundary conditions apply.

The lower plot depicts the result obtained by the universal filter function. The agreement between the two plots is good.

At first glance, these results are quite surprising because the ULF method is based on perturbation theory. In particular, the expression (85) for the universal filter function $\Gamma_{\text{uni}}(r)$ is obtained for high temperatures or small potential fluctuations. One can expect that the perturbative approach must be restricted to parameter sets that correspond to small density fluctuations. However, it is seen that the approach works well even when the density varies by more than an order of magnitude.

We surmise that the surprising success of the effective potential in describing the local particle density at fairly low temperatures, $T \gtrsim 0.2T_0$, is related to the fact that $n(\mathbf{r}, T)$ depends on $W(\mathbf{r}, T)$ exponentially. As in statistical physics, the error appears to be proportional to higher-order cumulants in the expansion in $V(\mathbf{r})/T$. Cumulants often decay faster with temperature than the corresponding coefficients of the bare series expansion because n th-order cumulants describe true n -point correlations that cannot be factorized into smaller subclusters.

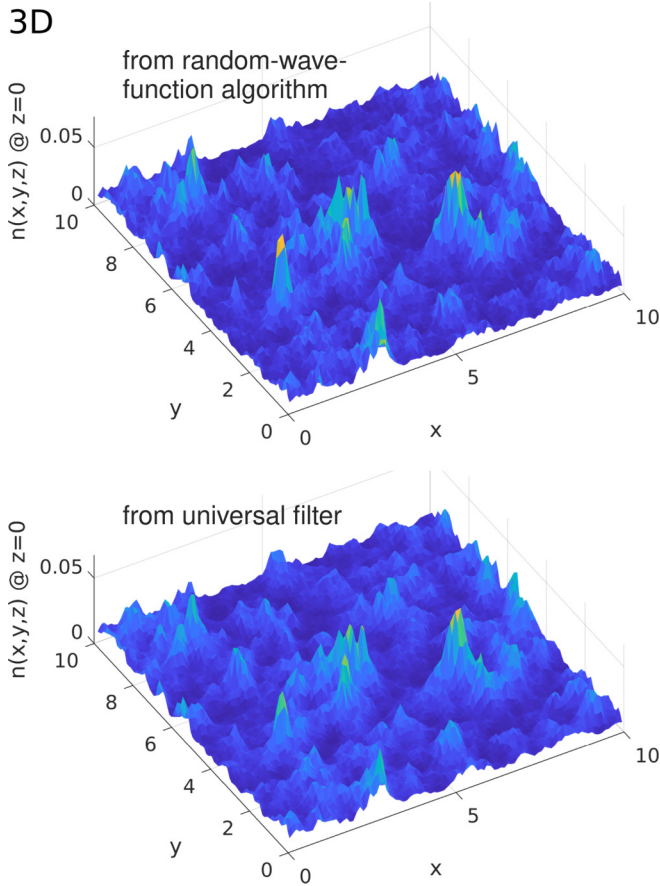


FIG. 14. Comparison between the exact electron density $n(x, y, z = 0, T)$ (upper part) and that obtained by using the universal filter function (lower part) in a three-dimensional white-noise potential. The sample size is $10 \times 10 \times 10$ dimensionless units, the discretization parameter is $a = 0.1$, the temperature is $T = 2$, the particle concentration is $n = 0.01$. Periodic boundary conditions apply.

IV. COMPARISON WITH LOCALIZATION-LANDSCAPE THEORY (LLT)

In this section, we compare our results to those obtained from the LLT for the charge carrier concentration $n(\mathbf{r}, T)$. In addition, we discuss the consequences of the different approximate techniques of calculating $n(\mathbf{r}, T)$ for charge transport in disordered media at elevated temperatures.

The aim of the potential filtering with the ULF developed in Sec. III and that of the RWF approach developed in Sec. II is to speed up calculations compared to solving the Schrödinger equation. The same aim has been targeted in the recently developed LLT [2,11–14].

A. Localization-landscape theory

In the LLT, the right-hand side of the Schrödinger equation is replaced with a constant to arrive at the landscape equation

$$\hat{H}u(\mathbf{r}) = \left(-\frac{\hbar^2}{2m} \nabla^2 + V(\mathbf{r}) \right) u(\mathbf{r}) = 1, \quad (90)$$

where $V(\mathbf{r})$ is the disorder potential and $u(\mathbf{r})$ is localization landscape for appropriate boundary conditions. The inverse of the landscape, $W(\mathbf{r}) \equiv 1/u(\mathbf{r})$, can be interpreted as a semi-classical effective confining potential that determines the strength of the confinement as well as the long-range decay of the quantum states.

1. Positivity condition

An important condition for the applicability of the LLT is that the Hamiltonian \hat{H} is a positive operator [12]. When solving the Schrödinger equation (2), the potential $V(\mathbf{r})$ experienced by the quantum particle can be defined up to a constant K . If one shifts the potential by K , then the resulting eigenenergies ϵ_i are shifted by the same constant K . However, this invariance does not hold for the landscape $u(\mathbf{r})$. If $u(\mathbf{r})$ is the solution to Eq. (90), then the solution $u_K(\mathbf{r})$ corresponding to the same potential shifted by the constant K satisfies [12]

$$-\frac{\hbar^2}{2m} \Delta u_K(\mathbf{r}) + [V(\mathbf{r}) + K]u_K(\mathbf{r}) = 1, \quad (91)$$

and $u(\mathbf{r}) \neq u_K(\mathbf{r})$ for general $K \neq 0$. In the LLT, the constant K is chosen as small as possible in such a way that the Hamiltonian remains a positive operator [12], and the electron density $n(\mathbf{r}, T)$ should be obtained from the effective potential $W_K(\mathbf{r}) \equiv 1/u_K(\mathbf{r})$ via Eq. (49).

Below we discuss that the choice of K drastically affects the predictions of the LLT approach. In the calculations below, we choose $K = -1.05V_{\min}$, where V_{\min} is the absolute minimum of $V(\mathbf{r})$.

2. Computational effort

The exact, complete solution of the Schrödinger equation is computationally demanding for large systems, and approximate techniques are mandatory for random media in two and three dimensions. The RWF requires the repeated application of the Hamiltonian onto a random wave function. The time consumption of the latter approach depends on the system size and on the number of realization used for the averaging procedure. Therefore, the accuracy of the RWF approach can be systematically improved by increasing the number of stored wave functions and realizations of the impurity potentials for the price of increasing computational resources. Thus, mesoscopically large systems cannot be treated using the RWF.

The LLT is based on a solution of a system of linear equations. Compared to solving the Schrödinger equation self-consistently, the LLT speeds up the calculations by two to three orders of magnitude [31]. However, the ULF approach requires only Fast Fourier Transformation, which does not consume noticeable computational time. Below we compare the accuracy of all three approximate approaches in $d = 1$ and $d = 2$ and show that the ULF is superior to the LLT not only in speed but also in precision.

B. Temperature-dependent particle density

In this subsection, we first focus on the electron density in a one-dimensional setting. The LLT is seen to work very well for temperatures $T \gtrsim T_0$ but the results deteriorate quickly for $T \lesssim 0.5T_0$. Second, we investigate two dimensions where

the bare LLT predicts too sharp and pronounced maxima and minima even at $T = T_0$.

The LLT problem can be cured by a Gaussian broadening of the random potential $V(\mathbf{r})$ before the LLT is applied. Such a broadening has been used by Piccardo *et al.* [13] and by Li *et al.* [14] to smoothen the rapidly changing distribution of atoms and to obtain a continuous fluctuating potential. Unfortunately, the optimal broadening parameter $\sigma(T)$ depends on temperature and is not known *a priori*.

1. Carriers on a chain

In Sec. III D 4, we compared exact and approximate results using the universal filtering in $d = 1$ dimension. Let us now compare these data with the LLT predictions for $n(x, T)$ at temperatures $T = 0.2, 0.5, 1, 2$ at $n = 0.01$.

In Fig. 15 we plot the results of the LLT along with the exact solution and with the ULF results copied from Fig. 12. Remarkably, the higher the temperature T , the better the agreement between the three approaches. Above $T = 1$, the agreement can be considered as perfect with respect to both, the number of extrema and the values $n(x, T)$. At $T = 0.5$, the LLT predicts much more extrema and a broader distribution for $n(x, T)$ in comparison with the exact solution and the ULF approach. At $T = 0.2$ and below, the disagreement between the LLT and the exact solution increases drastically.

We conclude that the LLT is a reliable approach in $d = 1$ at temperatures $T \gtrsim T_0$, though not at $T < T_0$. Recall that $T_0 \equiv \varepsilon_0/k_B$, where ε_0 is the energy scale of the disorder potential. To give an example, let us consider an InGaN multi-quantum-well solar-cell structures designed for photo-carrier collection [2]. Using the estimate $\varepsilon_0 \approx 20$ meV from the energy slope of the Urbach tail [2], we arrive at the estimate $T_0 \approx 230$ K for the temperature below which the LLT approach fails to describe the spatial distribution of the electron concentration.

2. Carriers on a square lattice

In Fig. 16(a), we show the electron density $n(x, y, T)$ in $d = 2$ at $T = T_0$, obtained from the LLT with $K = 18.2$ in units of ε_0 applied to the random potential $V(x, y)$ used for calculations of $n(x, y, T)$ in Fig 13. Apparently, the electron density provided by the LLT in Fig. 16(a) substantially deviates from $n(x, y, T)$ in Fig 13. The LLT predicts a series of narrow peaks in the electron density distribution with amplitudes that are one order of magnitude larger than the values of $n(x, y, T)$ given by the exact solution.

In Fig. 16(b), we show the electron density $n(x, y, T)$ in $d = 2$ at $T = T_0$, obtained by the application of the LLT to the random potential $V(x, y)$ smoothed by a Gaussian averaging. The averaging is a convolution between $V(x, y)$ and a Gaussian function $\exp[-(x^2 + y^2)/(2\sigma^2)]$. Such a procedure has been previously used by Piccardo *et al.* [13] and by Li *et al.* [14] to smoothen the rapidly changing distribution of atoms and to obtain a continuous fluctuating potential. The smoothed potential allows a choice of the constant K in Eq. (91) that is much smaller than that for the bare random potential $V(x, y)$ because the distribution of the potential values narrows after the Gaussian smoothing. For the case of $V(x, y)$ used to generate Fig. 16(a), the choice $K = 5.1$ warrants a positive

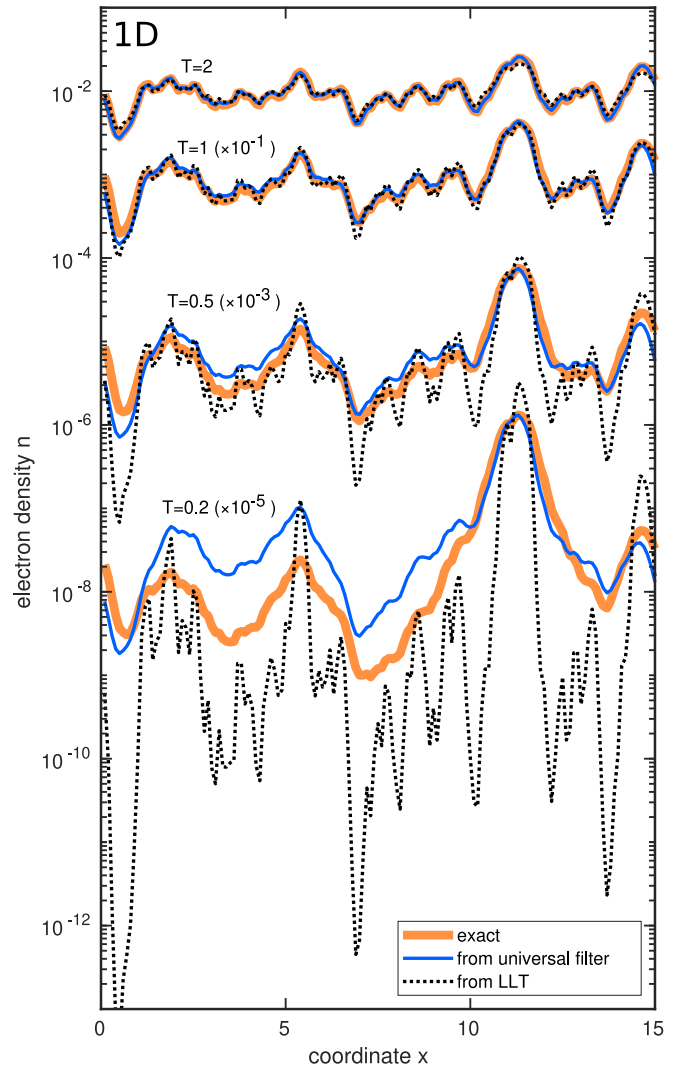


FIG. 15. Comparison between the exact electron density $n(x, T)$ (solid orange lines) and that obtained using the ULF function (solid blue lines) and the LLT (dashed black line) in a one-dimensional white-noise potential at different temperatures T . The parameters are the same as in Fig. 1, except for the temperature T . For clarity, the curves related to $T = 0.2$, $T = 0.5$, and $T = 1$ are multiplied by 10^{-5} , 10^{-3} , and 10^{-1} , respectively, as indicated in the plot. The particle concentration is $n = 0.01$.

Hamiltonian for the smoothed potential for which we choose $\sigma = 1.5a$.

To preserve the disorder effects on the electronic properties, the length scale of the averaging must be smaller or comparable to the typical scale of the effective potential fluctuations seen by the carriers [13,14]. Piccardo *et al.* [13] and Li *et al.* [14] fixed the Gaussian broadening parameter to a value of $\sigma = 2a_{\text{cat}} \approx 0.6$ nm, where a_{cat} is the average distance between cations in GaN studied by Piccardo *et al.* [13]. We varied the broadening parameter to achieve the best agreement between the LLT result and the exact solution for $n(x, y, T)$ in $d = 2$ at $T = T_0$. In Fig. 16(b), the electron density $n(x, y, T)$ is shown for the optimal value of the broadening parameter $\sigma = 1.5a$, where a is the distance between the grid points.

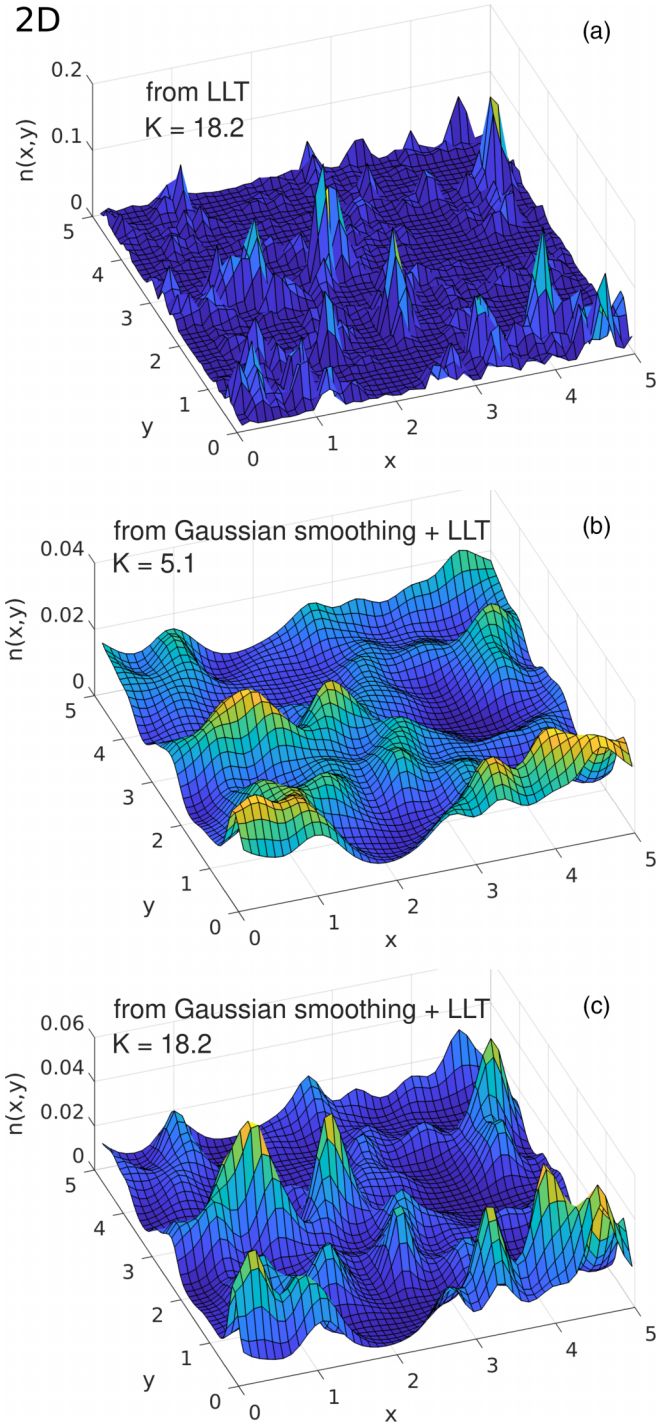


FIG. 16. Electron density $n(x, y, T)$ obtained using the LLT approach with different parameters σ in units a and K in units ε_0 , as described in the text. (a) $\sigma = 0$, $K = 18.2$; (b) $\sigma = 1.5$, $K = 5.1$; (c) $\sigma = 1.5$, $K = 18.2$. Other parameters are the same as in Fig. 13.

Apparently, it is possible to achieve the correct electron density $n(x, y)$ in the framework of the LLT, provided the optimal broadening parameter for the Gaussian averaging of the bare random potential $V(x, y)$ is known. However, in lack of an exact solution, there is no recipe in the framework of the LLT for how to get access to this optimal averaging parameter. Further below, we shall give an heuristic estimate for $\sigma(T)$.

The question arises whether the difference in the spatial distributions of the electron density in Figs. 16(a) and 16(b) is caused by the potential averaging itself, or by the different choices of the constant K . To resolve this question, we perform the calculations of $n(x, y, T)$ with the same smoothing of $V(x, y)$ as used for the data in Fig. 16(b) and the value $K = 18.2$ as used for the data in Fig. 16(a). The results are plotted in Fig. 16(c). The distribution $n(x, y, T)$ in Fig. 16(c) drastically deviates from the correct result in Fig. 13. This underlines the importance of the constant K in Eq. (91) for the predictions of the LLT approach. While smoothing $V(x, y)$ with $\sigma = 1.5a$ and using $K = 5.1$ yields the correct distribution $n(x, y)$ for the given realization $V(x, y)$, other choices for σ and K fail to reproduce the correct $n(x, y)$.

C. Semiclassical transport

As a second application, we compare the predictions of RWF, ULF, and LLT for semi-classical transport.

1. Transport in one dimension

First, we address the consequences of the various approaches to the electron density $n(x, T)$ for the charge carrier mobility in one-dimensional disordered systems. For simplicity, we assume a constant, spatially independent value μ_0 for the local mobility [8].

Since we have a series of local resistors, we address the local resistivity that is given by

$$\rho(x, T) = \frac{1}{e\mu_0 n(x, T)}. \quad (92)$$

The sample average gives

$$\bar{\rho}(T) \equiv \langle \rho(x, T) \rangle = \frac{1}{e\mu_0} \langle n^{-1}(x, T) \rangle. \quad (93)$$

By definition of the macroscopic mobility we have

$$\bar{\rho}(T) = \frac{1}{e\mu_{\text{eff}}(T) \langle n(x, T) \rangle}. \quad (94)$$

A comparison of Eqs. (93) and (94) provides the following compact result for the macroscopic mobility $\mu_{\text{eff}}(T)$

$$\mu_{\text{eff}}(T) = \frac{\mu_0}{\langle n(x, T) \rangle \langle n^{-1}(x, T) \rangle}. \quad (95)$$

In one dimension, the macroscopic mobility follows from the average of the local particle density and of its inverse.

In Fig. 17 we show the exact result for the temperature-dependent carrier mobility $\mu_{\text{eff}}(T)$ in comparison with those from the various approximate approaches. At $T \geq T_0$ all results practically coincide. The RWF is the only approximate approach that reliably reproduces $\mu_{\text{eff}}(T)$ down to temperatures, $T \approx 0.1T_0$. The results of the ULF approach start to deviate from the exact solution around $T = 0.25T_0$ but those of the LLT method begin to fail already at $T = 0.8T_0$, showing that the ULF is superior to the LLT in accuracy, at smaller computational cost. Note, however, that for very small temperatures, $T \lesssim 0.2T_0$, the ULF is also inadequate for the mobility in one-dimensional systems.

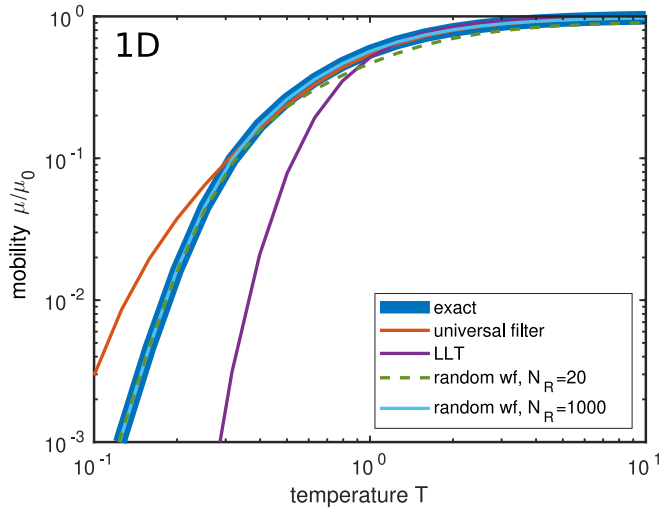


FIG. 17. Temperature-dependent charge carrier mobility in one dimension. We compare exact results with those from the RWF, ULF, and LLT approximations to calculate the average of the local density $n(x, T)$ and of its inverse. N_R denotes the number of realizations used for averaging in the RWF algorithm.

2. Transport on a square lattice from percolation theory

In dimensions $d \geq 2$, the calculation of $\mu_{\text{eff}}(T)$ poses a percolation problem [1]. In essence, the percolation approach requires to find the smallest value $\zeta_c(T)$ that provides a connected path via areas with local conductivity $\zeta(x, y, T) \geq \zeta_c(T)$. The value $\zeta_c(T)$ is to be considered as the macroscopic conductivity of the system [1] that characterizes the long-range charge transport.

Percolation theory predicts that in $d = 2$ the area corresponding to the inequality $\zeta(x, y, T) \geq \zeta_c(T)$ is exactly one half of a total system area [36]. Herewith, $\zeta_c(T)$ is the median of the distribution $\zeta(x, y, T)$. The local conductivity is determined by the local electron concentration $n(x, y, T)$,

$$\zeta(x, y, T) = e\mu_0 n(x, y, T), \quad (96)$$

while the macroscopic conductivity $\zeta_c(T)$ is determined by the average concentration $\langle n(x, y, T) \rangle$,

$$\zeta_c(T) = e\mu_{\text{eff}}(T) \langle n(x, y, T) \rangle. \quad (97)$$

The latter equation yields the relation

$$\mu_{\text{eff}}(T) = \mu_0 \frac{\overline{n(x, y, T)}}{\langle n(x, y, T) \rangle}, \quad (98)$$

where $\overline{n(x, y, T)}$ denotes the median of the distribution $n(x, y, T)$.

In Fig. 18 we show the results for the temperature-dependent carrier mobility $\mu_{\text{eff}}(T)$ in two dimensions given by Eq. (98) as obtained from the different schemes for calculating the average and the median of $n(x, T)$. The RWF and the ULF provide reliable results down to $T = 0.1T_0$, the results of the LLT deviate from the exact data already at $T = 5T_0$. The agreement becomes slightly better when a Gaussian averaging is applied to the disorder potential $V(x, y)$ before the LLT is applied, see Sec. IV B 2. When the Gaussian broadening $\sigma = 1.5a$ and the constant $K = 5.1\epsilon_0$ are used in

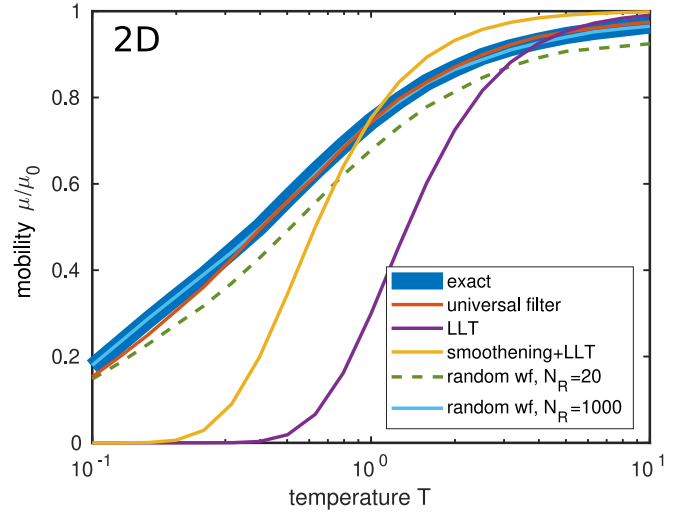


FIG. 18. Temperature-dependent charge carrier mobility in two dimensions. We compare exact results from percolation theory with those from the RWF, ULF, and LLT approximations to calculate the average of the local density $n(x, T)$ and of its median. N_R denotes the number of realizations used for averaging in the RWF algorithm. LLT results with and without Gaussian smoothing.

Eq. (91) so that the distribution $n(x, y)$ is reproduced from LLT at $T = T_0$ as seen in Sec. IV B 2, also the value of $\mu_{\text{eff}}(T)/\mu_0$ calculated via Eq. (98) is reproduced at $T = T_0$ but not at any other temperature. This strengthens the conclusion that the choice of the Gaussian broadening parameter σ and the choice of the constant K in the LLT equation (91) must depend on temperature to bring the result in agreement with the exact solution.

Heuristically, we find that the choice $\sigma(T) \sim T^{-0.75}$ provides acceptable results in two dimensions for the mobility $\mu_{\text{eff}}(T)$. After smoothing, we set $K = -1.05\tilde{V}_{\text{min}}$, where $\tilde{V}(x, y)$ is the random potential after Gaussian smoothing with its absolute minimum \tilde{V}_{min} .

V. DISCUSSION AND CONCLUSIONS

The theoretical description of the optoelectronic properties of disordered media requires an accurate knowledge of the space-dependent and temperature-dependent charge carrier distribution $n(\mathbf{r}, T)$ in the presence of a random potential. Two methods are currently available to determine $n(\mathbf{r}, T)$: (i) solving the Schrödinger equation and (ii) utilizing the LLT [11–14]. While exact, the complete solution of the Schrödinger equation is extremely demanding with respect to computational time and computer memory. It is hardly affordable for applications to realistically large, chemically complex systems. As exemplified in Sec. IV, the LLT is valid only in certain cases with unspecific limits. These limits can be revealed only by comparison with the exact solution of the Schrödinger equation for particles in a random potential $V(\mathbf{r})$.

In this work, we propose two novel theoretical tools, the RWF algorithm and the ULF approach, that permit an approximate calculation of $n(\mathbf{r}, T)$ without solving the Schrödinger equation. In comparison, both methods require less computational resources than the complete solution of the Schrödinger

equation, and both have a better accuracy and a broader range of applicability than the LLT.

As shown in this work, the RWF approach is as accurate and generally applicable to nondegenerate electron systems as solving the Schrödinger equation. However, for practical applications at temperatures $T \gtrsim 0.1T_0$, the RWF is much less demanding with respect to computational resources than solving the Schrödinger problem. Nevertheless, even the RWF becomes computationally too costly for mesoscopically large three-dimensional systems at low temperatures. For example, the calculations of $n(\mathbf{r}, T)$ depicted in Fig. 14 consumed 1.5 h on a PC in the case of the RWF approach but only 0.15 s in the case of the ULF scheme.

The ULF approach employs the temperature-dependent effective potential $W(\mathbf{r}, T)$. In this respect it is similar to the LLT, which also relies on a quasiclassical potential that replaces the random potential $V(\mathbf{r})$. However, the effective potential $W(\mathbf{r}, T)$ in the ULF approach depends on temperature, while the effective potential in LLT is temperature-independent. In Figs. 7 and 9, it is clearly seen that the effective potential responsible for the distribution $n(\mathbf{r}, T)$ strongly depends on temperature to reproduce the exact solution. Sec. IV provides evidence that ignoring the T -dependence of the effective potential $W(\mathbf{r}, T)$ prevents an accurate calculation of the electron distribution $n(\mathbf{r}, T)$. In the ULF, a universal low-pass filter is applied to the potential $V(\mathbf{r})$ via Eq. (62). We derive this linear filter analytically using high-temperature perturbation theory. The filter is T -dependent, while T does not enter Eq. (90) of the LLT.

The numerical tests performed in Sec. IV show that the range of applicability for the ULF approach is much broader than that for the LLT. Furthermore, the ULF scheme requires only Fast Fourier Transformation which is computationally much less demanding than solving the LLT Eq. (90) so that mesoscopically large three-dimensional disordered systems appear within reach for temperatures $T \gtrsim 0.5T_0$.

The space- and temperature-dependent electron distribution $n(\mathbf{r}, T)$ is the key ingredient for the theoretical treatment of charge transport. In our work it is shown that RWF and ULF provide a solid basis for the theoretical treatment of charge transport in disordered media.

In this paper, the calculation of the equilibrium carrier density in the Boltzmann approximation is considered for a disordered potential as a function of temperature. However, in practice, there are many problems where the carrier distribution at low temperature is not in equilibrium. Although neither RWF nor ULF can be applied to nonequilibrium problems straightforwardly, there is a perspective to possible modification of RWF to make it applicable to nonequilibrium cases. If the number of realizations N_R decreases, then the calculated occupation of energy levels by electrons gradually deviates from their equilibrium values. In principle, these deviations may mimic the nonequilibrium distributions, and one could interpret the green dashed lines in Figs. 1 and 4 as corresponding to the nonequilibrium electron densities. However, two problems arise in such interpretation of the calculated results. First, the deviations from the equilibrium occupation should be more pronounced for the low-energy states than for the high-energy levels. Some modifications of RWF should be performed to fulfill this condition. Second, the occupations

of energy levels in RWF are described by χ^2 distribution, while in reality another statistics holds. For instance, the occupations should obey Poisson statistics in the approximation of noninteracting electrons. More research is necessary to overcome these obstacles.

ACKNOWLEDGMENTS

A.V.N. thanks the Faculty of Physics of the Philipps Universität Marburg for the kind hospitality during his research stay. S.D.B. and K.M. acknowledge financial support by the Deutsche Forschungsgemeinschaft (Research Training Group ‘‘TIDE,’’ RTG2591) as well as by the key profile area ‘‘Quantum Matter and Materials (QM2)’’ at the University of Cologne. K.M. further acknowledges support by the DFG through the project ASTRAL (Grant No. ME1246-42).

APPENDIX A: ACCURACY OF THE RANDOM-WAVE-FUNCTION ALGORITHM

The aim of this section is to derive expression (34) for the expected value of $[\Delta(\mathbf{r})]^2$. Dividing the numerator and the denominator by $e^{\beta\mu}$ in Eq. (33), and taking Eqs. (9) and (32) into account, we obtain

$$\Delta(\mathbf{r}) = \frac{N_R^{-1} \sum_{\mathbf{R}} [\tilde{n}_{\mathbf{R}}(\mathbf{r}) - \tilde{n}(\mathbf{r})]}{\tilde{n}(\mathbf{r})}. \quad (\text{A1})$$

As shown in Sec. II B,

$$\langle \tilde{n}_{\mathbf{R}}(\mathbf{r}) \rangle = \tilde{n}(\mathbf{r}), \quad (\text{A2})$$

where angle brackets stand for the expected value. Substituting this result into Eq. (A1), one can ensure that

$$\langle \Delta(\mathbf{r}) \rangle = 0. \quad (\text{A3})$$

Hence,

$$\begin{aligned} \langle [\Delta(\mathbf{r})]^2 \rangle &= \text{var } \Delta(\mathbf{r}) \\ &= \frac{\text{var} \{ \sum_{\mathbf{R}} [\tilde{n}_{\mathbf{R}}(\mathbf{r}) - \tilde{n}(\mathbf{r})] \}}{N_R^2 [\tilde{n}(\mathbf{r})]^2} \\ &= \frac{\sum_{\mathbf{R}} \text{var} \{ [\tilde{n}_{\mathbf{R}}(\mathbf{r}) - \tilde{n}(\mathbf{r})] \}}{N_R^2 [\tilde{n}(\mathbf{r})]^2} \\ &= \frac{\text{var} \{ [\tilde{n}_{\mathbf{R}}(\mathbf{r}) - \tilde{n}(\mathbf{r})] \}}{N_R [\tilde{n}(\mathbf{r})]^2} \\ &= \frac{\langle [\tilde{n}_{\mathbf{R}}(\mathbf{r})]^2 \rangle - [\tilde{n}(\mathbf{r})]^2}{N_R [\tilde{n}(\mathbf{r})]^2}, \end{aligned} \quad (\text{A4})$$

where symbol ‘‘var’’ denotes variance, and we use the fact that variance of the sum is equal to the sum of variances of independent variables.

Then we recall that $\tilde{n}_{\mathbf{R}}(\mathbf{r})$ is a square of random quantity $\gamma_{\mathbf{R}}(\mathbf{r}) \equiv \sqrt{2}\psi_{\mathbf{R}}(\mathbf{r})$ according to Eq. (23). The latter quantity is, by construction, a linear combination of Gaussian random variables $c_{i,R}^{(0)}$, and therefore has a Gaussian distribution with expected value zero. The expected value of $\tilde{n}_{\mathbf{R}}(\mathbf{r})$ is the second moment of $\gamma_{\mathbf{R}}(\mathbf{r})$, and the expected value of $[\tilde{n}_{\mathbf{R}}(\mathbf{r})]^2$ is the fourth moment of $\gamma_{\mathbf{R}}(\mathbf{r})$. Due to Wick’s probability theorem, the fourth moment of a normally distributed random variable is three times larger than the square of its second moment.

Hence,

$$\langle [\tilde{n}_R(\mathbf{r})]^2 \rangle = 3[\tilde{n}(\mathbf{r})]^2. \quad (\text{A5})$$

Finally, substitution of Eq. (A5) into Eq. (A4) gives

$$\langle [\Delta(\mathbf{r})]^2 \rangle = \frac{2}{N_R}. \quad (\text{A6})$$

APPENDIX B: CONSTANT PARAMETER AT SMALL DISCRETIZATION

In this Appendix we show how to derive the scaling form (67) for the constant parameter $C(T)$.

We start from Eq. (49) that expresses the electron density $n(\mathbf{r}, T)$ through the effective potential $W(\mathbf{r}, T)$,

$$\begin{aligned} n(\mathbf{r}, T) &= N_c e^{\beta[\mu - W(\mathbf{r}, T)]} \\ &= N_c e^{\beta\mu} \left[1 - \beta W(\mathbf{r}, T) + \frac{\beta^2}{2} W^2(\mathbf{r}, T) - \dots \right]. \end{aligned} \quad (\text{B1})$$

Since we consider the potential $V(\mathbf{r})$ as a small perturbation, we expand $n(\mathbf{r}, T)$ and $W(\mathbf{r}, T)$ in a power series,

$$n(\mathbf{r}, T) = n_0(T) + n_1(\mathbf{r}, T) + n_2(\mathbf{r}, T) + \mathcal{O}(V^3), \quad (\text{B2})$$

$$W(\mathbf{r}, T) = W_1(\mathbf{r}, T) + W_2(\mathbf{r}, T) + \mathcal{O}(V^3), \quad (\text{B3})$$

where $n_0(T) = N_c \exp(\beta\mu)$. Here, $n_1(\mathbf{r}, T)$ and $W_1(\mathbf{r}, T)$ are linear in V , and $n_2(\mathbf{r}, T)$ and $W_2(\mathbf{r}, T)$ are quadratic in V . Substituting Eq. (B2) into Eq. (B1), and collecting the terms up to quadratic order in V , we obtain

$$n_2(\mathbf{r}, T) = N_c e^{\beta\mu} \left[\frac{\beta^2}{2} W_1^2(\mathbf{r}, T) - \beta W_2(\mathbf{r}, T) \right], \quad (\text{B4})$$

where the filter function defines the linear relation between the random potential and the effective potential,

$$W_1(\mathbf{r}, T) = \int d\mathbf{r}' \Gamma(\mathbf{r}', T) V(\mathbf{r} + \mathbf{r}'), \quad (\text{B5})$$

see Eqs. (62) and (81).

Equation (66) shows that $C(T) = \langle W(\mathbf{r}) \rangle - \langle V(\mathbf{r}) \rangle$. The odd powers of the white-noise potential V vanish after averaging, hence

$$C(T) = \langle W_2(\mathbf{r}, T) \rangle + \mathcal{O}(V^4). \quad (\text{B6})$$

We substitute $W_2(\mathbf{r}, T)$ using Eq. (B4) into Eq. (B6) and neglect the residual term $\mathcal{O}(V^4)$ to obtain

$$C(T) = C^{(1)}(T) + C^{(2)}(T), \quad (\text{B7})$$

with the two contributions

$$\begin{aligned} C^{(1)}(T) &= \frac{\beta}{2} \langle W_1^2(\mathbf{r}, T) \rangle, \\ C^{(2)}(T) &= - \frac{\langle n_2(\mathbf{r}, T) \rangle}{\beta N_c e^{\beta\mu}}. \end{aligned} \quad (\text{B8})$$

1. First contribution

The mean value of $W_1^2(\mathbf{r}, T)$ in Eq. (B8) depends on the statistics of the random potential $V(\mathbf{r})$. For a white-noise

potential, Eq. (38) leads to

$$\langle W_1^2(\mathbf{r}, T) \rangle = S \int d\mathbf{r}' [\Gamma(\mathbf{r}', T)]^2, \quad (\text{B9})$$

which is indeed independent of \mathbf{r} . Here, the parameter S characterizes the strength of the potential fluctuations. The Fourier image of the filter function,

$$\hat{\Gamma}(\mathbf{k}) = \int d\mathbf{r} \Gamma(\mathbf{r}) e^{i\mathbf{k}\cdot\mathbf{r}}, \quad (\text{B10})$$

permits us to rewrite Eq. (B9) using the Plancherel identity with the result

$$C^{(1)}(T) = \frac{\beta S}{2(2\pi)^d} \int d\mathbf{k} [\hat{\Gamma}(\mathbf{k})]^2. \quad (\text{B11})$$

Here, $d = 1, 2, 3$ is the spacial dimension. Using Eq. (89), we express $\hat{\Gamma}(\mathbf{k})$ via the universal function $\hat{\Gamma}_{\text{uni}}(k)$, which is defined by Eq. (87). The resulting coefficients $C^{(1)}(T)$ are

$$\begin{aligned} C_{1d}^{(1)}(T) &= \frac{\beta S}{4\pi\tilde{\lambda}} \int_{-\infty}^{\infty} \left[\frac{\sqrt{\pi}}{k} e^{-k^2/4} \text{erfi}(k/2) \right]^2 dk \\ &\approx 0.260 \frac{\beta S}{\tilde{\lambda}} \end{aligned} \quad (\text{B12})$$

in $d = 1$ dimension,

$$\begin{aligned} C_{2d}^{(1)}(T) &= \frac{\beta S}{2(2\pi\tilde{\lambda})^2} \int_0^{\infty} 2\pi k \left[\frac{\sqrt{\pi}}{k} e^{-k^2/4} \text{erfi}(k/2) \right]^2 dk \\ &\approx 0.146 \frac{\beta S}{\tilde{\lambda}^2} \end{aligned} \quad (\text{B13})$$

in $d = 2$ dimensions, and

$$\begin{aligned} C_{3d}^{(1)}(T) &= \frac{\beta S}{2(2\pi\tilde{\lambda})^3} \int_0^{\infty} 4\pi k^2 \left[\frac{\sqrt{\pi}}{k} e^{-k^2/4} \text{erfi}(k/2) \right]^2 dk \\ &\approx 0.0971 \frac{\beta S}{\tilde{\lambda}^3} \end{aligned} \quad (\text{B14})$$

in $d = 3$ dimensions.

2. Second contribution

To calculate $C^{(2)}(T)$, we need an expression for the second-order correction $n_2(\mathbf{r}, T)$ to the electron density $n(\mathbf{r}, T)$. We start from Eq. (72) that expresses the electron density through the one-particle Hamiltonian \hat{H} ,

$$n(\mathbf{r}, T) = 2e^{\beta\mu} \langle \mathbf{r} | \exp(-\beta\hat{H}) | \mathbf{r} \rangle. \quad (\text{B15})$$

Let us consider the kinetic-energy operator \hat{T} as the nonperturbed Hamiltonian, and the potential-energy operator

$$\hat{V} = \int d\mathbf{r} V(\mathbf{r}) |\mathbf{r}\rangle \langle \mathbf{r}| \quad (\text{B16})$$

as a small perturbation. Then, the perturbation expansion up to the second order yields

$$n(\mathbf{r}, T) = n_0(T) + n_1(\mathbf{r}, T) + n_2(\mathbf{r}, T),$$

$$n_0(T) = 2e^{\beta\mu} \langle \mathbf{r} | e^{-\beta\hat{T}} | \mathbf{r} \rangle,$$

$$n_1(\mathbf{r}, T) = -2e^{\beta\mu} \int_0^{\beta} d\xi \langle \mathbf{r} | e^{-\xi\hat{T}} \hat{V} e^{(\xi-\beta)\hat{T}} | \mathbf{r} \rangle,$$

$$n_2(\mathbf{r}, T) = 2e^{\beta\mu} \int_0^\beta d\xi_1 \int_{\xi_1}^\beta d\xi_2 \times \langle \mathbf{r} | e^{-\xi_1 \hat{T}} \hat{V} e^{(\xi_1 - \xi_2) \hat{T}} \hat{V} e^{(\xi_2 - \beta) \hat{T}} | \mathbf{r} \rangle. \quad (\text{B17})$$

As our next step, we insert the expression for \hat{V} from Eq. (B16) into Eq. (B17) to see that

$$n_2(\mathbf{r}, T) = \iint d\mathbf{r}_1 d\mathbf{r}_2 \Gamma_n^{(2)}(\mathbf{r}_1, \mathbf{r}_2, T) V(\mathbf{r} + \mathbf{r}_1) V(\mathbf{r} + \mathbf{r}_2), \quad (\text{B18})$$

where the kernel $\Gamma_n^{(2)}(\mathbf{r}_1, \mathbf{r}_2, T)$ is defined by

$$\Gamma_n^{(2)}(\mathbf{r}_1, \mathbf{r}_2, T) = 2e^{\beta\mu} \int_0^\beta d\xi_1 \int_{\xi_1}^\beta d\xi_2 \langle \mathbf{0} | e^{-\xi_1 \hat{T}} | \mathbf{r}_1 \rangle \times \langle \mathbf{r}_1 | e^{(\xi_1 - \xi_2) \hat{T}} | \mathbf{r}_2 \rangle \langle \mathbf{r}_2 | e^{(\xi_2 - \beta) \hat{T}} | \mathbf{0} \rangle. \quad (\text{B19})$$

The expression (B8) for $C^{(2)}(T)$ contains the mean value of $n_2(\mathbf{r}, T)$. Using Eq. (B18) and the statistics of the white-noise potential $V(\mathbf{r})$ from Eq. (38) we obtain the average value in the form

$$\langle n_2(\mathbf{r}, T) \rangle = S \int d\mathbf{r}' \Gamma_n^{(2)}(\mathbf{r}', \mathbf{r}', T), \quad (\text{B20})$$

which is independent of \mathbf{r} . To calculate the integral on the right-hand side, we represent the kinetic-energy operator \hat{T} in Fourier space as

$$\hat{T} = \frac{\Omega}{(2\pi)^d} \int d\mathbf{k} \frac{\hbar^2 k^2}{2m} |\mathbf{k}\rangle \langle \mathbf{k}|, \quad (\text{B21})$$

and we use Eq. (80) for the plane-wave matrix elements $\langle \mathbf{r} | \mathbf{k} \rangle$. Then Eq. (B19) leads to

$$\int d\mathbf{r} \Gamma_n^{(2)}(\mathbf{r}, \mathbf{r}, T) = \frac{2e^{\beta\mu}}{(2\pi)^{3d}} \int_0^\beta d\xi_1 \int_{\xi_1}^\beta d\xi_2 \times \iiint d\mathbf{k}_1 d\mathbf{k}_2 d\mathbf{k}_3 \int d\mathbf{r} \times e^{-\hbar^2 \xi_1 k_1^2 / (2m)} e^{\hbar^2 (\xi_1 - \xi_2) k_2^2 / (2m)} \times e^{\hbar^2 (\xi_2 - \beta) k_3^2 / (2m)} e^{i(\mathbf{k}_3 - \mathbf{k}_1) \cdot \mathbf{r}}. \quad (\text{B22})$$

Here, the integration over \mathbf{r} is straightforward,

$$\int d\mathbf{r} e^{i(\mathbf{k}_3 - \mathbf{k}_1) \cdot \mathbf{r}} = (2\pi)^d \delta(\mathbf{k}_3 - \mathbf{k}_1), \quad (\text{B23})$$

which allows us to perform the integral over \mathbf{k}_3 . Thence,

$$\begin{aligned} & \int d\mathbf{r} \Gamma_n^{(2)}(\mathbf{r}, \mathbf{r}, T) \\ &= \frac{2e^{\beta\mu}}{(2\pi)^{2d}} \int_0^\beta d\xi_1 \int_{\xi_1}^\beta d\xi_2 \left(\int d\mathbf{k}_1 e^{-(\beta - \xi_2 + \xi_1) \hbar^2 k_1^2 / (2m)} \right) \\ & \quad \times \left(\int d\mathbf{k}_2 e^{-(\xi_2 - \xi_1) \hbar^2 k_2^2 / (2m)} \right) \\ &= \frac{2e^{\beta\mu}}{(2\pi)^{2d}} \int_0^\beta d\xi_1 \int_{\xi_1}^\beta d\xi_2 \left(\frac{2\pi m}{(\beta - \xi_2 + \xi_1) \hbar^2} \right)^{d/2} \\ & \quad \times \left(\frac{2\pi m}{(\xi_2 - \xi_1) \hbar^2} \right)^{d/2}. \end{aligned} \quad (\text{B24})$$

In the latter expression, the parameters ξ_1 and ξ_2 appear only in the combination $\xi = \xi_2 - \xi_1$. To further simplify the integrals, we note that, for any function $\phi(\xi)$,

$$\int_0^\beta d\xi_1 \int_{\xi_1}^\beta d\xi_2 \phi(\xi_2 - \xi_1) = \int_0^\beta d\xi (\beta - \xi) \phi(\xi) \quad (\text{B25})$$

holds. Hence,

$$\begin{aligned} \int d\mathbf{r} \Gamma_n^{(2)}(\mathbf{r}, \mathbf{r}, T) &= 2e^{\beta\mu} \left(\frac{m}{2\pi \hbar^2} \right)^d \\ & \quad \times \int_0^\beta d\xi \xi^{-d/2} (\beta - \xi)^{1-d/2}. \end{aligned} \quad (\text{B26})$$

We combine Eqs. (B8), (B20), and (B26), and express N_c from Eq. (47) and λ from Eq. (64) to arrive at a simple formula for the constant $C^{(2)}(T)$,

$$C^{(2)}(T) = -\frac{S\beta^{d-1}}{(2\sqrt{\pi}\lambda)^d} \int_0^\beta d\xi \xi^{-d/2} (\beta - \xi)^{1-d/2}. \quad (\text{B27})$$

In $d = 1$ dimension, this formula is readily evaluated,

$$C_{1d}^{(2)}(T) = -\frac{\sqrt{\pi}}{4} \frac{S\beta}{\lambda}, \quad (\text{B28})$$

because the integral converges.

However, the integral in Eq. (B27) diverges in two and three dimensions. In particular,

$$C_{2d}^{(2)}(T) = -\frac{S\beta}{4\pi\lambda^2} \int_0^\beta \frac{d\xi}{\xi}. \quad (\text{B29})$$

This divergence stems from the divergent integral

$$I(\xi) = \int d\mathbf{k} \exp\left(-\xi \frac{\hbar^2 |\mathbf{k}|^2}{2m}\right), \quad (\text{B30})$$

that appears in Eq. (B24). This integral becomes infinitely large in the limit $\xi \rightarrow 0$ when the integration is performed over the whole \mathbf{k} -space. However, in a discretized model, the value of $|\mathbf{k}|$ cannot be larger than $\simeq a^{-1}$, where a is the grid lattice constant. This shows that the lower limit of the integral in Eq. (B29) should be set to

$$\xi_{\min} \simeq \frac{1}{\epsilon_{\max}} \simeq \frac{ma^2}{\hbar^2} \simeq \frac{a^2\beta}{\lambda^2}. \quad (\text{B31})$$

Therefore, in two dimensions we find

$$C_{2d}^{(2)}(T) = \frac{S\beta}{2\pi\lambda^2} \ln \frac{\tilde{\mu}_2 a}{\lambda}, \quad (\text{B32})$$

where $\tilde{\mu}_2$ arises from the unknown proportionality factor between the left-hand side and the right-hand side of Eq. (B31). The factor μ_2 may depend also on the type of the discretization grid (square, hexagonal, etc.).

Similarly, we replace the lower limit in Eq. (B27) by ξ_{\min} also in three dimensions,

$$C_{3d}^{(2)}(T) = -\frac{S\beta}{(4\pi)^{3/2}\lambda^3} \left[2\sqrt{\frac{\beta}{\xi_{\min}}} + \mathcal{O}\left(\frac{\xi_{\min}}{\beta}\right) \right]. \quad (\text{B33})$$

Neglecting the last term in the square brackets and substituting ξ_{\min} from Eq. (B31), we find

$$C_{3d}^{(2)}(T) = -\mu_3 \frac{S\beta}{\lambda^2 a}, \quad (\text{B34})$$

where the parameter μ_3 again depends on the undetermined factor in Eq. (B31).

3. Summary

Summing up the expressions for $C^{(1)}(T)$, Eqs. (B12)–(B14), and for $C^{(2)}(T)$, Eqs. (B28), (B32), and (B34), we arrive at the following results for the coefficient $C(T)$ in $d = 1, 2, 3$ dimensions,

$$C_{1d}(T) = -0.183 \frac{S}{k_B T \tilde{\lambda}}, \quad (\text{B35})$$

$$C_{2d}(T) = \frac{S}{k_B T \tilde{\lambda}^2} \frac{1}{2\pi} \ln \frac{\mu_2 a}{\tilde{\lambda}}, \quad (\text{B36})$$

$$C_{3d}(T) = \frac{S}{k_B T \tilde{\lambda}^3} \left(-\mu_3 \frac{\tilde{\lambda}}{a} + 0.0971 \right). \quad (\text{B37})$$

The parameters μ_2 and μ_3 in these formulas are lattice specific and can be found by fitting of the numerical data. As shown in the main text, $\mu_2 \approx 0.30$ for the square lattice, and $\mu_3 \approx 0.255$ for the three-dimensional cubic lattice. Thus, Eq. (67) is shown to hold within second-order perturbation theory for a white-noise random potential.

-
- [1] Edited by S. D. Baranovskii, *Charge Transport in Disordered Solids with Applications in Electronics* (John Wiley and Sons, Chichester, UK, 2006).
- [2] C. Weisbuch, S. Nakamura, Y.-R. Wu, and J. S. Speck, Disorder effects in nitride semiconductors: Impact on fundamental and device properties, *Nanophotonics* **10**, 3 (2021).
- [3] Z. Hu, Z. Lin, J. Su, J. Zhang, J. Chang, and Y. Hao, A review on energy band-gap engineering for perovskite photovoltaics, *Solar RRL* **3**, 1900304 (2019).
- [4] S. D. Baranovskii, P. Höhbusch, A. V. Nenashev, A. V. Dvurechenskii, M. Gerhard, D. Hertel, K. Meerholz, M. Koch, and F. Gebhard, Comment on Interplay of structural and optoelectronic properties in formamidinium mixed tin-lead triiodide perovskites, *Adv. Funct. Mater.* **32**, 2201309 (2022).
- [5] A. Chaves, J. G. Azadani, H. Alsalmán, D. R. da Costa, R. Frisenda, A. J. Chaves, S. H. Song, Y. D. Kim, D. He, J. Zhou, A. Castellanos-Gomez, F. M. Peeters, Z. Liu, C. L. Hinkle, S.-H. Oh, P. D. Ye, S. J. Koester, Y. H. Lee, P. Avouris, X. Wang *et al.*, Bandgap engineering of two-dimensional semiconductor materials, *npj 2D Mater. Appl.* **4**, 29 (2020).
- [6] H. Masenda, L. M. Schneider, M. Adel Aly, S. J. Machchhar, A. Usman, K. Meerholz, F. Gebhard, S. D. Baranovskii, and M. Koch, Energy scaling of compositional disorder in ternary transition-metal dichalcogenide monolayers, *Adv. Electron. Mater.* **7**, 2100196 (2021).
- [7] K. Nomura, H. Ohta, A. Takagi, T. Kamiya, M. Hirano, and H. Hosono, Room-temperature fabrication of transparent flexible thin film transistors using amorphous oxide semiconductors, *Nature (London)* **432**, 488 (2004).
- [8] A. V. Nenashev, J. O. Oelerich, S. H. M. Greiner, A. V. Dvurechenskii, F. Gebhard, and S. D. Baranovskii, Percolation description of charge transport in amorphous oxide semiconductors, *Phys. Rev. B* **100**, 125202 (2019).
- [9] B. I. Halperin and M. Lax, Impurity-band tails in the high-density limit. I. Minimum counting methods, *Phys. Rev.* **148**, 722 (1966).
- [10] S. D. Baranovskii and A. L. Efros, Band edge smearing in solid solutions, *Sov. Phys. Semicond.* **12**, 1328 (1978).
- [11] D. N. Arnold, G. David, D. Jerison, S. Mayboroda, and M. Filoche, Effective Confining Potential of Quantum States in Disordered Media, *Phys. Rev. Lett.* **116**, 056602 (2016).
- [12] M. Filoche, M. Piccardo, Y.-R. Wu, C.-K. Li, C. Weisbuch, and S. Mayboroda, Localization Landscape Theory of disorder in semiconductors. I. Theory and modeling, *Phys. Rev. B* **95**, 144204 (2017).
- [13] M. Piccardo, C.-K. Li, Y.-R. Wu, J. S. Speck, B. Bonaf, R. M. Farrell, M. Filoche, L. Martinelli, J. Peretti, and C. Weisbuch, Localization Landscape Theory of disorder in semiconductors. II. Urbach tails of disordered quantum well layers, *Phys. Rev. B* **95**, 144205 (2017).
- [14] C.-K. Li, M. Piccardo, L.-S. Lu, S. Mayboroda, L. Martinelli, J. Peretti, J. S. Speck, C. Weisbuch, M. Filoche, and Y.-R. Wu, Localization landscape theory of disorder in semiconductors. III. Application to carrier transport and recombination in light emitting diodes, *Phys. Rev. B* **95**, 144206 (2017).
- [15] H.-H. Chen, J. S. Speck, C. Weisbuch, and Y.-R. Wu, Three-dimensional simulation on the transport and quantum efficiency of UVC-LEDs with random alloy fluctuations, *Appl. Phys. Lett.* **113**, 153504 (2018).
- [16] A. Di Vito, A. Pecchia, A. Di Carlo, and M. Auf der Maur, Simulating random alloy effects in III-nitride light emitting diodes, *J. Appl. Phys.* **128**, 041102 (2020).
- [17] J. A. Gonzalez Montoya, A. Tibaldi, C. De Santi, M. Meneghini, M. Goano, and F. Bertazzi, Nonequilibrium Green's Function Modeling of Trap-Assisted Tunneling in $\text{In}_x \text{Ga}_{1-x} \text{N}/\text{GaN}$ Light-Emitting Diodes, *Phys. Rev. Appl.* **16**, 044023 (2021).
- [18] A. Tibaldi, J. A. Gonzalez Montoya, M. Vallone, M. Goano, E. Bellotti, and F. Bertazzi, Modeling Infrared Superlattice Photodetectors: From Nonequilibrium Green's Functions to Quantum-Corrected Drift Diffusion, *Phys. Rev. Appl.* **16**, 044024 (2021).
- [19] D. Chaudhuri, M. O'Donovan, T. Streckenbach, O. Marquardt, P. Farrell, S. K. Patra, T. Koprucki, and S. Schulz, Multiscale simulations of the electronic structure of III-nitride quantum wells with varied indium content: Connecting atomistic and continuum-based models, *J. Appl. Phys.* **129**, 073104 (2021).
- [20] H.-T. Shen, C. Weisbuch, J. S. Speck, and Y.-R. Wu, Three-dimensional Modeling of Minority-Carrier Lateral Diffusion Length Including Random Alloy Fluctuations in $(\text{In}, \text{Ga})\text{N}$ and $(\text{Al}, \text{Ga})\text{N}$ Single Quantum Wells, *Phys. Rev. Appl.* **16**, 024054 (2021).
- [21] H.-T. Shen, Y.-C. Chang, and Y.-R. Wu, Analysis of light-emission polarization ratio in deep-ultraviolet light-emitting

- diodes by considering random alloy fluctuations with the 3d $k\text{\AA}\cdot p$ method, *Phys. Status Solidi RRL* **16**, 2100498 (2022).
- [22] T.-Y. Tsai, K. Michalczewski, P. Martyniuk, C.-H. Wu, and Y.-R. Wu, Application of Localization Landscape Theory and the $k\text{-}p$ model for direct modeling of carrier transport in a type-II superlattice InAs/InAsSb photoconductor system, *J. Appl. Phys.* **127**, 033104 (2020).
- [23] Y. C. Chow, C. Lee, M. S. Wong, Y.-R. Wu, S. Nakamura, S. P. DenBaars, J. E. Bowers, and J. S. Speck, Dependence of carrier escape lifetimes on quantum barrier thickness in InGaN/GaN multiple quantum well photodetectors, *Opt. Express* **28**, 23796 (2020).
- [24] W. Liu, G. Rossbach, A. Avramescu, T. Schimpke, H.-J. Lugauer, M. Strassburg, C. Mounir, U. T. Schwarz, B. Deveaud, and G. Jacopin, Impact of alloy disorder on Auger recombination in single InGaN/GaN core-shell microrods, *Phys. Rev. B* **100**, 235301 (2019).
- [25] S. S. Shamilov, D. J. Brown, T. A. Haase, and M. D. Hoogerland, Computing the eigenstate localisation length at very low energies from localisation landscape theory, *SciPost Phys. Core* **4**, 017 (2021).
- [26] J. Zhan, Z. Chen, C. Li, Y. Chen, J. Nie, Z. Pan, C. Deng, X. Xi, F. Jiao, X. Kang, S. Li, Q. Wang, T. Yu, Y. Tong, G. Zhang, and B. Shen, Investigation on many-body effects in micro-LEDs under ultra-high injection levels, *Opt. Express* **29**, 13219 (2021).
- [27] F. Bertazzi, A. Tibaldi, M. Goano, Jesus Alberto Gonzalez Montoya, and E. Bellotti, Nonequilibrium Green's Function Modeling of Type-II Superlattice Detectors and Its Connection to Semiclassical Approaches, *Phys. Rev. Appl.* **14**, 014083 (2020).
- [28] M. O'Donovan, D. Chaudhuri, T. Streckenbach, P. Farrell, S. Schulz, and T. Koprucki, From atomistic tight-binding theory to macroscale drift diffusion: Multiscale modeling and numerical simulation of uni-polar charge transport in (In,Ga)N devices with random fluctuations, *J. Appl. Phys.* **130**, 065702 (2021).
- [29] M. O'Donovan, P. Farrell, T. Streckenbach, T. Koprucki, and S. Schulz, Multiscale simulations of uni-polar hole transport in (In,Ga)N quantum well systems, *Opt. Quantum Electron.* **54**, 405 (2022).
- [30] J.-P. Banon, P. Pelletier, C. Weisbuch, S. Mayboroda, and M. Filoche, Wigner-weyl description of light absorption in disordered semiconductor alloys using the localization landscape theory, *Phys. Rev. B* **105**, 125422 (2022).
- [31] Y. Liu, J.-P. Banon, K. Frohna, Y.-H. Chiang, G. Tumen-Ulzii, S. D. Stranks, M. Filoche, and R. H. Friend, The electronic disorder landscape of mixed halide perovskites, *ACS Energy Lett.* **8**, 250 (2023).
- [32] F. Gebhard, A. V. Nenashev, K. Meerholz, and S. D. Baranovskii, Quantum states in disordered media. I. Low-pass filter approach, *Phys. Rev. B* **107**, 064206 (2023).
- [33] J. Lu and S. Steinerberger, Detecting localized eigenstates of linear operators, *Res. Math. Sci.* **5**, 33 (2018).
- [34] M. E. Raikh, S. D. Baranovskii, and B. I. Shklovskii, Dimensional quantization in a-Si:H quantum-well structures: The alloy model, *Phys. Rev. B* **41**, 7701 (1990).
- [35] S. Steinerberger, Regularized potentials of Schrödinger operators and a local landscape function, *Commun. Partial Diff. Eqs.* **46**, 1262 (2021).
- [36] B. I. Shklovskii and A. L. Efros, *Electronic Properties of Doped Semiconductors* (Springer, Berlin, 1984).